# Nonlinear Wrench Observer of an Underactuated Aerial Manipulator

YiZhuang Garrard\* and Wenlong Zhang<sup>†</sup>
Robotics and Intelligent Systems Laboratory, School of Manufacturing Systems and Networks, Arizona State University,
Mesa, AZ 85212, USA

Daisaku Inoyama<sup>‡</sup> and Tom Stoumbos<sup>§</sup>
Northrop Grumman Corporation, Space Systems, Dulles, Virginia, USA

Unmanned aerial manipulators have been growing in popularity over the years, alongside the complexity of the tasks they undertake. Many of these tasks include physical interaction with the environment, where a force control or sensing component is desirable. In these types of applications, the forces and torques, or the wrench, acting on the robot by the environment must be known. This paper presents a wrench observer based on an Extended Kalman filter, and compares it against acceleration-based, momentum-based, and hybrid wrench observers. Simulations using each of these observers are conducted with an underactuated aerial manipulator composed of a hexarotor with coplanar propellers and a 2-DOF manipulator. Measurement noise on par with what is expected in real-world applications is added to the sensor signals, and results show that the Extended Kalman filter-based wrench observer is superior at noise reduction and wrench estimation in many cases compared to the other observers.

### I. Introduction

Aerial robots are receiving significant attention in tasks that encompass a large workspace, such as search and rescue, mapping, and surveillance. Unmanned aerial manipulators (UAMs), or aerial vehicles with at least one robot arm, augment those abilities by being able to manipulate objects in the environment, such as sensor placement and removal ([1]), non-destructive testing ([2, 3]), and writing ([4]). In these tasks, the end-effector is often in contact with the environment, and knowledge of the interaction forces and torques, or wrench, is needed to accomplish those tasks. One method to obtain interaction wrench information is to install a force/torque sensor on the vehicle. Alternatively, the interaction wrench can be estimated from a wrench observer.

Wrench observers are used when force/torque sensors are not cost-effective, too heavy, or cannot be mounted where the interaction wrench will occur. Early works on fixed-base manipulators use momentum-based methods to estimate the external wrench about the robot joints ([5, 6]), requiring only joint positions and velocities. The use of momentum-based wrench estimation is extended to unmanned aerial vehicles (UAVs) by ([7–10]) for underactuated UAVs. A related work using disturbance observers to compensate for ground effect is shown in [11]. Momentum-based wrench estimation is also used on fully actuated UAVs for object pick-and-place ([12]) and human-UAV interaction ([13]). Fully actuated UAMs utilizing the same approach are shown in [14], [15], and [3].

[16] proposed a hybrid wrench observer for multirotor UAVs that built on the momentum-based observer, that relied only on the linear accelerations and angular velocity information available on the onboard inertial measurement unit (IMU). The hybrid wrench observer utilized the linear acceleration to estimate the external forces, while the angular velocity is used to estimate the torques via the momentum-based observer. This eliminates the need of numerically integrating the acceleration to obtain velocity. Other works that utilize hybrid wrench observer are [17] for pick-and-place operations, [18] for aerial screwing, and [19] for discriminating between contact and aerodynamic forces.

Lyapunov-based, quasi-static, and Extended Kalman Filter (EKF)-based wrench observers are also shown in literature. [20] provided a Lyapunov stability proof for a wrench observer for a quadrotor with a rigidly attached tool. The wrench only depends on velocity and position information, and is utilized to maintain a desired contact force with targets of different stiffnesses. [21] performed wrench estimation using a quasi-static hexarotor model with a

<sup>\*</sup>Graduate Student, Ira A. Fulton Schools of Engineering

<sup>&</sup>lt;sup>†</sup>Associate Professor, Ira A. Fulton Schools of Engineering

<sup>\*</sup>Manager, Tactical Space Systems Division, Dulles, VA 20166, AIAA Member

<sup>§</sup>Manager, Tactical Space Systems Division, Dulles, VA 20166, AIAA Associate Fellow

1-DOF arm that is kept horizontal. [22] used an EKF to perform wrench estimation on an aerial manipulator with a fully actuated floating base in simulation, and showed superior performance compared to momentum-based and hybrid wrench observers when sensor noise is present. However, the motion controller used by [22] was a perfect compensator against the external wrench, so the impact of the vehicle motion was not shown. Additionally, the wrench estimate in operational space is not shown.

In this paper, we present an EKF-based wrench observer and compare it against acceleration-based, momentum-based, and hybrid wrench observers. Simulation cases show the performance of these observers when external forces and torques are applied directly to the multirotor body and robot joints, as well as when an external torque is applied to the end-effector. Noise is added to the measurement signals to show how they affect the wrench estimates. A motion controller is used to keep the UAM in the air after external loads are applied. We show that after all the observers are tuned to settle within 10% of the external load within 3 seconds, the EKF-based observer is the most effective at reducing noise from the noisiest wrench estimates in both joint-space and operational space, and provides the most accurate estimates in operational space.

The rest of the paper is as follows: Section II describes the kinematics and differential kinematics of the aerial manipulator; Section III describes the dynamics of the aerial manipulator. Section IV describes the motion controller used to drive the robot. Section V describes the development of the acceleration-based, momentum-based, hybrid, and EKF-based wrench observer. In Section VI, the wrench observer is evaluated in simulation. Finally, Section VII concludes the paper and proposes future directions to extend the work.

# **II. Kinematics**

Let the inertial frame be expressed as  $\{I\}$ , the body frame  $\{B\}$  be placed in the geometric center of the multirotor body, and the frame  $\{E\}$  be placed at the Tool Center Point (TCP) of the end-effector, as shown in Fig. 1. The position of  $\{B\}$  with respect to  $\{I\}$  is given by the vector  $\boldsymbol{p}_B = \begin{bmatrix} x_B & y_B & z_B \end{bmatrix}^T$ , and the orientation of  $\{B\}$  with respect to  $\{I\}$  is given by the rotation matrix

$$\mathbf{R}_{B}(\boldsymbol{\varphi}_{B}) = \mathbf{R}_{z}(\psi_{B})\mathbf{R}_{v}(\theta_{B})\mathbf{R}_{x}(\phi_{B}),\tag{1}$$

where  $\mathbf{R}_z$ ,  $\mathbf{R}_y$ , and  $\mathbf{R}_x$  correspond to the rotation matrices about the z, y, and x axes, respectively, and  $\varphi_B = \begin{bmatrix} \psi_B & \theta_B & \phi_B \end{bmatrix}^T$  are the ZYX yaw-pitch-roll Euler angles. The pose of the multirotor body  $\{B\}$  with respect to  $\{I\}$  is given by

$$\boldsymbol{H}_{B}(\boldsymbol{p}_{B},\boldsymbol{\varphi}_{B}) = \begin{bmatrix} \boldsymbol{R}_{B} & \boldsymbol{p}_{B} \\ \boldsymbol{0}_{1\times3} & 1 \end{bmatrix}. \tag{2}$$

The homogenous transformation matrix of the end-effector with respect to the multirotor body is given by

$$H_E^B(q) = H_1^B(q_0)H_2^1(q_1)\cdots H_E^n(q_n),$$
 (3)

where n is the number of joints of the robot arm and  $q \in \mathbb{R}^n$  is the vector of joint coordinates. The pose of  $\{E\}$  with respect to  $\{I\}$  is given by

$$H_E(p_B, \varphi_B, q) = H_B(p_B, \varphi_B)H_E^B(q)$$
(4)

The velocity of  $\{E\}$  with respect to  $\{B\}$ ,

$$\mathbf{v}_{E}^{B} = \begin{bmatrix} \dot{\mathbf{p}}_{E}^{BT} & \omega_{E}^{BT} \end{bmatrix}^{T}$$
, is given by

$$\mathbf{v}_E^B = \mathbf{J}_E^B(\mathbf{q})\dot{\mathbf{q}},\tag{5}$$

where  $J_E^B \in \mathbb{R}^{6 \times n}$  is the geometric Jacobian of the robot arm. The Jacobian contribution from  $\{B\}$  to  $\{E\}$  is given by

$$J_B(\mathbf{p}_B, \mathbf{\varphi}_B, \mathbf{q}) = \begin{bmatrix} I_{3\times3} & -S(\mathbf{R}_B \mathbf{p}_E^B) \\ \mathbf{0}_{3\times3} & I_{3\times3} \end{bmatrix}, \tag{6}$$

where  $p_E^B$  is the position of  $\{E\}$  with respect to  $\{B\}$  and  $S(\cdot)$  is the skew-symmetric matrix operator performing the cross product. The velocity of  $\{E\}$  in  $\{I\}$  is given by

$$\mathbf{v}_E = \mathbf{J}_B \mathbf{v}_B + \mathbf{J}_E \dot{\mathbf{q}} = \mathbf{J} \mathbf{T}(\boldsymbol{\varphi}_B) \dot{\boldsymbol{\xi}},\tag{7}$$

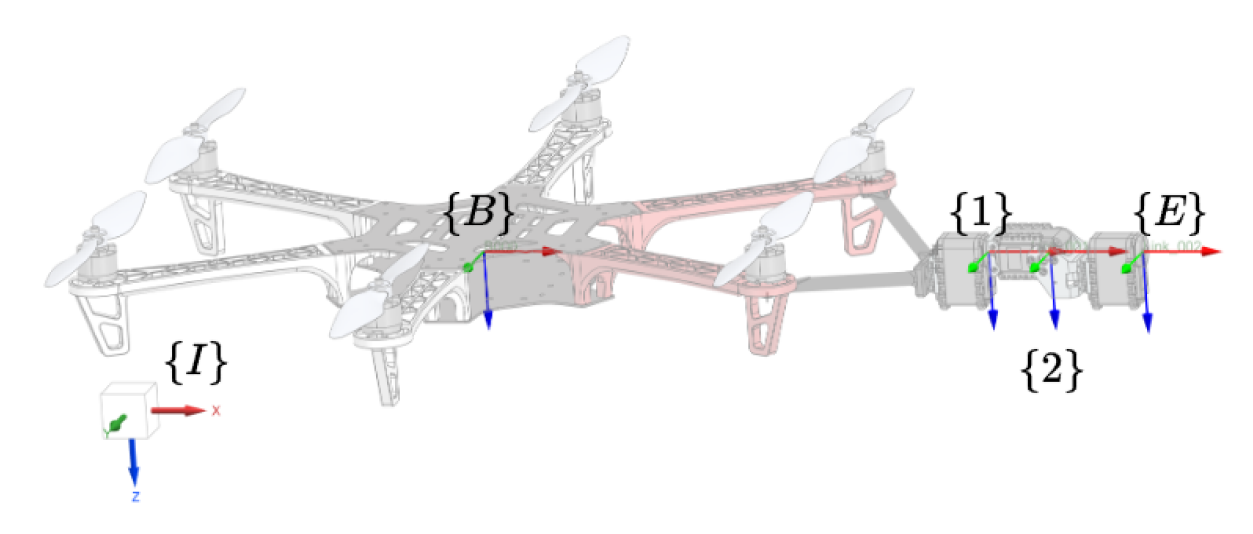


Fig. 1 Coordinate frames assigned to the aerial manipulator. External forces act along the x, y, and Z axes of  $\{B\}$  in  $\{I\}$ , torques along the x, y, and z axes of  $\{B\}$  in  $\{B\}$ , and the x-axis of  $\{1\}$ , and y-axis  $\{2\}$ .

where  $\mathbf{v}_B = \begin{bmatrix} \dot{\mathbf{p}}_B^T & \omega_B^T \end{bmatrix}^T$  is the linear and angular velocity of the multirotor body in  $\{I\}$ ,  $\mathbf{J} = \begin{bmatrix} \mathbf{J}_B & \mathbf{J}_E \end{bmatrix}$ ,  $\mathbf{\xi} = \begin{bmatrix} \mathbf{p}_B^T & \boldsymbol{\varphi}_B^T & \mathbf{q}^T \end{bmatrix}^T$  and

$$J_{E} = \begin{bmatrix} R_{B} & \mathbf{0}_{3\times3} \\ \mathbf{0}_{3\times3} & R_{B} \end{bmatrix} J_{E}^{B}, \qquad T = \begin{bmatrix} I_{3\times3} & \mathbf{0} & \mathbf{0} \\ \mathbf{0} & T_{B}(\varphi_{B}) & \mathbf{0} \\ \mathbf{0} & \mathbf{0} & I_{n\times n} \end{bmatrix}, \tag{8}$$

where

$$\begin{bmatrix} \omega_{x} \\ \omega_{y} \\ \omega_{z} \end{bmatrix} = \begin{bmatrix} -\sin\theta & 0 & 1 \\ \sin\phi\cos\theta & \cos\phi & 0 \\ \cos\phi\cos\theta & -\sin\phi & 0 \end{bmatrix} \begin{bmatrix} \dot{\psi} \\ \dot{\theta} \\ \dot{\phi} \end{bmatrix} = T_{B}(\varphi_{B})\dot{\varphi_{B}}$$
(9)

is the relationship between angular velocity  $\omega_B = \begin{bmatrix} \omega_x & \omega_y & \omega_z \end{bmatrix}^T$  in  $\{B\}$  and  $\dot{\varphi}_B$ .

# **III. Dynamics**

The equations of motion for the UAM can be derived using the Euler-Lagrange formulation shown by [23]:

$$M(\xi)\ddot{\xi} + C(\xi,\dot{\xi})\dot{\xi} + G(\xi) = u + w_{\rho}, \tag{10}$$

where  $M \in \mathbb{R}^{(6+n)\times(6+n)}$  is the symmetric and positive definite inertia matrix of the system,  $C \in \mathbb{R}^{(6+n)\times(6+n)}$  is the Coriolis matrix,  $G \in \mathbb{R}^{6+n}$  is the gravity vector,  $u \in \mathbb{R}^{6+n}$  is the vector of control inputs, and  $w_e \in \mathbb{R}^{6+n}$  is the external wrench applied to the robot in joint-space. For convenience later in the paper, let M be viewed as

$$M(\xi) = \begin{bmatrix} M_p \\ M_{\varphi} \\ M_q \end{bmatrix} = \begin{bmatrix} M_{pp} & M_{p\varphi} & M_{pq} \\ M_{\varphi p} & M_{\varphi \varphi} & M_{\varphi q} \\ M_{qp} & M_{q\varphi} & M_{qq} \end{bmatrix}, \tag{11}$$

where  $\boldsymbol{M}_{pp} \in \mathbb{R}^{3\times3}$ ,  $\boldsymbol{M}_{p\varphi} = \boldsymbol{M}_{\varphi p}^T \in \mathbb{R}^{3\times3}$ ,  $\boldsymbol{M}_{pq} = \boldsymbol{M}_{qp}^T \in \mathbb{R}^{3\times n}$ ,  $\boldsymbol{M}_{\varphi \varphi} \in \mathbb{R}^{3\times3}$ ,  $\boldsymbol{M}_{\varphi q} = \boldsymbol{M}_{q\varphi}^T \in \mathbb{R}^{3\times2}$ , and  $\boldsymbol{M}_{qq} \in \mathbb{R}^{n\times n}$ . Similarly,  $\boldsymbol{C}$  can be viewed as

$$C(\xi, \dot{\xi}) = \begin{bmatrix} C_p \\ C_{\varphi} \\ C_q \end{bmatrix} = \begin{bmatrix} C_{pp} & C_{p\varphi} & C_{pq} \\ C_{\varphi p} & C_{\varphi \varphi} & C_{\varphi q} \\ C_{qp} & C_{q\varphi} & C_{qq} \end{bmatrix}, \tag{12}$$

where each block has the same dimension as in M. G, u, and  $w_e$  can be viewed as

$$G(\xi) = \begin{bmatrix} G_p \\ G_{\varphi} \\ G_q \end{bmatrix}, \qquad u = \begin{bmatrix} u_f \\ u_{\varphi} \\ u_q \end{bmatrix}, \qquad w_e = \begin{bmatrix} w_{e,f} \\ w_{e,\varphi} \\ w_{e,q} \end{bmatrix}, \tag{13}$$

where  $G_p \in \mathbb{R}^3$ ,  $G_{\varphi} \in \mathbb{R}^3$ ,  $G_q \in \mathbb{R}^n$ ,  $u_f \in \mathbb{R}^3$ ,  $u_{\varphi} \in \mathbb{R}^3$ ,  $u_q \in \mathbb{R}^n$ ,  $w_{e,f} \in \mathbb{R}^3$ ,  $w_{e,\varphi} \in \mathbb{R}^3$ , and  $w_{e,q} \in \mathbb{R}^n$ . The vectors  $u_f$  and  $u_{\varphi}$  can be mapped from  $\{I\}$  to  $\{B\}$  via

$$f_B = -\mathbf{R}_B(\varphi)e_3\mathbf{u}_f, \qquad \mathbf{u}_\omega = \mathbf{T}_B(\varphi)\mathbf{u}_\varphi \tag{14}$$

where  $f_B$  is the total thrust of the motors in the  $\{B\}$  frame,  $e_3 = \begin{bmatrix} 0 & 0 & 1 \end{bmatrix}^T$ , and  $u_{\omega}$  is the moment produced by the motors about  $\{B\}$ .

#### IV. Motion Controller

Since the UAM has an underactuated multirotor body, a cascaded controller where the outer position controller feeds into the inner attitude controller is used. The position controller drives  $p_B, \psi_B$ , and q. Based on the outer loop, a reference pitch and roll angles are computed, and the final joint control signals are computed in the inner loop.

#### A. Joint Position Control

Consider (10) without the external wrench:

$$u = M\alpha + C\dot{\xi} + G,\tag{15}$$

where  $\alpha$  is the auxiliary control signal used to drive the control signal u.  $\alpha$  is computed via

$$\alpha = \mathbf{K}_P \mathbf{e} + \mathbf{K}_D \dot{\mathbf{e}},\tag{16}$$

where  $e = \xi_r - \xi$  and  $\dot{e} = \dot{\xi}_r - \dot{\xi}$ , are the joint position and velocity errors, respectively, and  $K_P \in \mathbb{R}^{(6+n)\times(6+n)}$  and  $K_D \in \mathbb{R}^{(6+n)\times(6+n)}$  are positive-definite matrices.  $\xi_r$  and  $\dot{\xi}_r$  are the reference position and velocity joint values. The pitch and roll errors are set to zero at this point because their reference values cannot be computed until  $u_f$  is known.

## **B.** Attitude Control

The reference pitch and roll angles are computed based on  $u_f$  and the current  $\psi$ :

$$\xi_{r,\theta} = \tan\left(\frac{u_{f,x}\cos(\psi) + u_{f,y}\sin(\psi)}{u_{f,z}}\right)^{-1}$$

$$\xi_{r,\phi} = \sin\left(\frac{u_{f,y}\cos(\psi) - u_{f,x}\sin(\psi)}{||\mathbf{u}_f||}\right)^{-1},$$

$$(17)$$

$$\xi_{r,\phi} = \sin\left(\frac{u_{f,y}\cos(\psi) - u_{f,x}\sin(\psi)}{||u_f||}\right)^{-1},\tag{18}$$

where  $||\cdot||$  indicates the 2-norm The errors are recomputed and used in (15) and (16) to get the final control forces and torques for the multirotor and manipulator.

# V. Wrench Observer

One method of obtaining external wrench estimates is to install a force/torque sensor on the end-effector, with the tradeoffs being that the external wrench can only be measured at a single point on the robot, increased cost, and increased weight. Alternatively, a wrench observer can be implemented, which provides an estimate of the interaction wrench at the TCP when accurate joint-space position, velocity, and acceleration information is available directly, through numerical integration or differentiation, or estimation.

Most wrench observers map the external wrench to the robot joint space [22, 24, 25]. Some wrench observers map the joint space wrench to the TCP, but these are limited to single-body robots [14, 20]. In this work, we are interested in the joint-space and operational-space estimates from wrench observers on a UAM. An acceleration-based, momentum-based, and hybrid wrench observers are introduced first as baseline approaches, then the EKF-based observer is developed, with the idea that the EKF-based method should reduce the noise present in the other approaches and have more accurate wrench estimates.

#### A. Acceleration-Based Wrench Observer

The acceleration-based wrench observer is based on the algebraic manipulation of the equations of motion. Starting with (10), the joint-space external wrench is

$$\mathbf{w}_e = \mathbf{M}\ddot{\mathbf{\xi}} + \mathbf{C}\dot{\mathbf{\xi}} + \mathbf{G} - \mathbf{u}. \tag{19}$$

The signal  $\xi$  contains noise, and if derivatives of  $\xi$  are required, the noise is amplified. To attenuate the noise, a first-order filter is used:

$$\dot{\widehat{w}}_e = K_A w_e - K_A w_e, \tag{20}$$

where  $K_A \in \mathbb{R}^{(6+n)\times(6+n)}$  is a positive-definite matrix. By substituting (19) into (20), we get

$$\dot{\widehat{w}}_e = K_A \left( M(\xi) \ddot{\xi} + C(\xi, \dot{\xi}) \dot{\xi} + G(\xi) - u - \widehat{w}_e \right). \tag{21}$$

To map the operational-space external wrench into joint-space, left-multiply (21) with  $(J^T)^{\dagger}$ , where  $(\cdot)^{\dagger}$  denotes the pseudoinverse.

# **B.** Momentum-Based Wrench Observer

The momentum-based observer utilizes knowledge of the UAM's momentum  $p = M\dot{\xi}$ , with the block view of p given as  $p = \begin{bmatrix} p_D^T & p_Q^T & p_Q^T \end{bmatrix}^T$ . Following [5], define a residual vector

$$\widehat{\mathbf{w}}_{e} = \mathbf{K}_{M} \left[ \mathbf{p} - \int \left( \mathbf{u} + \mathbf{C}^{T} \dot{\mathbf{\xi}} - \mathbf{G} + \widehat{\mathbf{w}}_{e} \right) dt - \mathbf{p}(0) \right], \tag{22}$$

where  $K_M \in \mathbb{R}^{(6+n)\times(6+n)}$  is a positive-definite matrix. Assuming that  $p(0) = \mathbf{0}$ , (22) simplifies to

$$\hat{\mathbf{w}}_e = \mathbf{K}_M \left[ \mathbf{p} - \int \left( \mathbf{u} + \mathbf{C}^T \dot{\mathbf{\xi}} - \mathbf{G} + \hat{\mathbf{w}}_e \right) dt \right]$$
 (23)

# C. Hybrid Wrench Observer

The hybrid wrench observer combines the acceleration-based method for forces and the momentum-based method for torques so that wrench estimates only use directly measurable values without the need for numerical integration or differentiation. While this functions well for single-body UAVs, the attached robot arm on a UAM couples position, velocity, and acceleration together. As such, forces and torques are no longer independent, and may negate the benefit of the hybrid wrench observer.

The hybrid wrench observer is given by the first three rows of (21) and the last 3 + n rows of (23):

$$\widehat{\mathbf{w}}_{e} = \mathbf{K}_{H} \begin{bmatrix} \int \left( \mathbf{M}_{p} \ddot{\boldsymbol{\xi}} + \mathbf{C}_{p} \dot{\boldsymbol{\xi}} + \mathbf{G}_{p} - \mathbf{u}_{f} - \widehat{\mathbf{w}}_{e,f} \right) dt \\ \mathbf{p}_{\varphi} \\ \mathbf{p}_{q} \end{bmatrix} - \int \left( \begin{bmatrix} \mathbf{u}_{\varphi} \\ \mathbf{u}_{q} \end{bmatrix} + \mathbf{C}_{m} \dot{\boldsymbol{\xi}} - \begin{bmatrix} \mathbf{G}_{\varphi} \\ \mathbf{G}_{q} \end{bmatrix} + \begin{bmatrix} \widehat{\mathbf{w}}_{e,\varphi} \\ \widehat{\mathbf{w}}_{e,q} \end{bmatrix} \right) dt \end{bmatrix}, \tag{24}$$

where

$$C_m = \begin{bmatrix} C_{p\varphi}^T & C_{\varphi\varphi}^T & C_{q\varphi}^T \\ C_{pq}^T & C_{\varphi q}^T & C_{qq}^T \end{bmatrix}$$
 (25)

# D. EKF-Based Wrench Observer

Let the process vector be

$$x = \begin{bmatrix} \xi \\ \dot{\xi} \\ w_e \end{bmatrix}. \tag{26}$$

The process vector contains the variables necessary for system propagation, and is augmented to include the external wrench.

The process noise and measurement noise are assumed to be white and Gaussian, and follow a probability distribution

$$n_p \sim \mathcal{N}(\mathbf{0}_{8\times 1}, N_p)$$
  

$$n_m \sim \mathcal{N}(\mathbf{0}_{8\times 1}, N_m),$$
(27)

where  $N_p \in \mathbb{R}^{(6+n)\times(6+n)}$  and  $N_m \in \mathbb{R}^{(6+n)\times(6+n)}$  are constant covariance matrices.

The state-transition function is formulated as

$$\dot{\mathbf{x}} = \mathbf{f}(\mathbf{x}, \mathbf{n}_p) = \begin{bmatrix} \dot{\mathbf{\xi}} \\ \mathbf{M}^{-1} \left( \mathbf{u} - \widehat{\mathbf{w}}_e - \mathbf{C}\dot{\mathbf{\xi}} - \mathbf{G} \right) \\ \mathbf{0}_{8 \times 1} \end{bmatrix} + \mathbf{n}_p.$$
 (28)

The derivative of the external wrench is set to zero, and will be corrected by the EKF in the correction step. Let the measurement vector be written as

$$y = \begin{bmatrix} \xi \\ \ddot{p}_B \\ \omega_B. \end{bmatrix} + n_m. \tag{29}$$

The measurement vector contains the variables that are directly measurable. It is assumed that  $\xi$  is available from sources such as motion capture systems and servo encoders, while  $\ddot{p}_B$  and  $\omega_B$  are acquired from the onboard IMU. The map from the process vector to  $\xi$  is directly obtainable from (26),  $\ddot{p}_B$  is given by the first three rows of  $M^{-1}$   $(u - \hat{w}_e - C\dot{\xi} - G)$ , and  $\omega_B$  is given by (9).

To implement the continuous-time equations (28) and (29) into an EKF, they are first discretized using a fourth-order Runge-Kutta method. The discretized equations are denoted

$$\hat{\mathbf{x}}_k = f(\hat{\mathbf{x}}_{k-1}, \mathbf{u}_k) \tag{30}$$

$$\hat{\mathbf{y}}_k = \mathbf{h}(\hat{\mathbf{x}}_k). \tag{31}$$

The EKF pseudocode is shown in Algorithm 1, where F and H are the Jacobian of (30) and (31), respectively, P is the covariance matrix, S is the innovation, and K is the Kalman gain. The subscript notation n|m indicates the estimated value at time step n given observations up to  $m \le n$ .

# Algorithm 1 EKF Pseudocode

```
\begin{split} & \text{Initialize:} \\ & \widehat{x}_{0|0} \leftarrow \widehat{x}_0 \\ & P_{0|0} \leftarrow P_0 \\ & \text{loop} \\ & \text{Prediction Step:} \\ & \widehat{x}_{k+1|k} \leftarrow f(\widehat{x}_{k|k}, u_k) \\ & P_{k+1|k} \leftarrow F_k P_{k|k} F_k^T + n_{p,k} \\ & y_{k+1|k} \leftarrow h(\widehat{x}_{k+1|k}) \\ & \text{Correction Step:} \\ & S_{k+1} \leftarrow H_{k+1} P_{k+1|k} H_{k+1}^T + n_{m,k} \\ & K_{k+1} \leftarrow P_{k+1|k} H_{k+1}^T S_{k+1}^{-1} \\ & \widehat{x}_{k+1|k+1} \leftarrow \widehat{x}_{k+1|k} + K_{k+1}(y_{k+1} - y_{k+1|k}) \\ & P_{k+1|k+1} \leftarrow P_{k+1|k} - K_{k+1} S_{k+1} K_{k+1}^T \\ & \text{end loop} \end{split}
```

# VI. Simulation

To show that performance between the acceleration-based, momentum-based, hybrid, and EKF-based wrench observers, a co-simulation setup is designed with Siemens Simcenter 3D (Siemens Digital Industries Software®, Plano, TX) and MATLAB Simulink (MathWorks®, Natick, MA). The geometry and mass properties of the UAM are set up in

**Table 1** Simcenter 3D Motion Solution Parameters

**Table 2** Simulation Gains

Analysis Options							
Print Interval Definition	Fixed Print Interval						
Fixed Print Interval	0.01 s						
Gravity	9806.65 mm/s <sup>2</sup>						
Dynamic Pr	operties						
Simulation Type	Co-Simulation						
Integration Method	PECE						
Communication Interval	0.01 s						
Max Integration Step	0.001 s						
Integration Tolerance	1e-6						
Solution Tolerance	1e-6						
Acceleration Tolerance	0.0001						
Solver Acceleration	Iterative						
Initial Valority Mathad	Moore-Penrose						
Initial Velocity Method	Pseudo Inverse						

Gain	Value								
$K_P$	diag(15, 15, 15, 200, 600, 400, 1500, 1000)								
$K_D$	diag(20, 20, 20, 30, 80, 80, 100, 100)								
$K_A$	$0.85I_{8\times8}$								
$K_{M}$	$0.85I_{8\times8}$								
$K_H$	$0.85I_{8\times8}$								
$P_0$	<b>0</b> <sub>24×24</sub>								
$N_P$	$\begin{bmatrix} 0_{16\times16} & 0_{16\times8} \\ 0_{8\times16} & 10^{-5} \mathbf{I}_{8\times8} \end{bmatrix}$								
$N_M$	$ \begin{bmatrix} 1I_{3\times3} & & & & \\ & 1I_{3\times3} & & & \\ & & 1I_{2\times2} & & & \\ & & & 15I_{3\times3} & & \\ & & & & 350I_{3\times3} \end{bmatrix} \times 10^{-3} $								

Simcenter 3D, and the control and wrench observers are implemented in Simulink. During simulation, the two software programs exchange sensor and control signals at 100 Hz.

The UAM multirotor body frame is modeled after that DJI Flame Wheel F550, with DJI 2212/920KV motors and 9450 propellers (DJI®, Nanshan District, Shenzhen). A PixRacer flight controller (Dronecode Project®, San Francisco, CA), Raspberry Pi 4b (Raspberry Pi Foundation®, Cambridge, England), and Arduino Due (Arduino®, Somerville, MA), are placed on the hexarotor frame. Custom attachments are made for the battery and robot arm. The robot arm is composed of three servos modeled after the Dynamixel AX-12A (ROBOTIS®, Lake Forest, CA) servos and their connecting structural elements. The first two servos are considered joints of the UAM, and the final servo is considered the tool.

The entire UAM is composed of three rigid bodies: the hexarotor frame along with the motors, electronics, attachments, and first servo body; the first servo horn through to the second servo body; and finally, the second servo horn to the end of the manipulator. These bodies coincide with  $\{B\}$ ,  $\{1\}$ , and  $\{2\}$  shown in Fig. 1. The axes of rotation for  $\{1\}$  and  $\{2\}$  are about their X and Y axes, respectively. The mass properties of each rigid body are computed using Simcenter 3D about frames  $\{B\}$ ,  $\{1\}$ , and  $\{2\}$ . These values are shown in For deriving the equations of motion Table 4, and are used to derive the equations of motion (10).

The parameters used for the Simcenter 3D solution are shown in Table 1.

All signals, blocks, and functions in Simulink run at 100 Hz, except for the inverse kinematics, which runs at 10 Hz. The Simulink solver runs with a fixed-step size of 0.01s using the discrete solver.

The Levenberg-Marquardt inverse kinematic algorithm is used to determine the joint positions for the motion controller to track. The only bounds specified for the algorithm are on  $\xi_{r,\theta}$  and  $\xi_{r,\phi}$ , both of which are fixed to their current values at every time step.

For both the motion controller and inverse kinematics, the true values of  $\xi$  are used, since directly using noisy signals brings the system closer to instability. Works such as [26] are suited for state estimation of UAMs. In this work, while the EKF-based wrench observer also yields  $\xi$  and  $\dot{\xi}$  estimates, the transient response is too slow to control the UAM.

The measurements used for wrench estimation are  $\xi$ ,  $\dot{\varphi}_B$ , and  $\ddot{p}_B$ . When the joint variables for wrench estimation or control are not directly available,  $\xi$ ,  $\dot{\varphi}$ , and  $\ddot{p}$  are numerically integrated or differentiated as necessary. Noise is added to the measurement signals based on Table 3 before any integration or differentiation. All differentiation and integration are done discretely; no continuous signals are used for control or estimation. The noise distribution is based on the default parameters for the PixRacer and the encoder resolution of the AX-12A.

Four test cases are developed to evaluate the wrench observers. In cases 1) and 2), external forces and torques exerted directly on  $\{B\}$  and the axes of rotation of  $\{1\}$  and  $\{2\}$ . Case 1) has nominal measurement noise as shown in

Table 3 Noise from sensors

Joints	Standard Deviation
$p_B$	0.001 m
$oldsymbol{arphi}_B$	0.011 <i>rad</i>
q	0.001 rad
$\dot{oldsymbol{arphi}}_B$	0.015 rad/s
$\ddot{p}_B$	$0.35 \ m/s^2$

**Table 4 Rigid Body Properties** 

Body	Mass (kg)	$I_{xx}, I_{yy}, I_{zz} (\text{kg-mm}^2)$					
Hexarotor	1.726	15536.950, 54661.920, 68965.179					
Link 1	0.054	8.378, 59.917, 62.084					
Link 2	0.063	27.159, 80.323, 67.032					

Table 3, while Case 2) doubles the standard deviation of the measurement noise. In both cases, 5N is applied to  $\{B\}$  with respect to each axis of  $\{I\}$ , and 2Nm is applied to each axis of  $\{B\}$  with respect to  $\{B\}$ . 0.1Nm is applied to the axes of rotation of  $\{1\}$  and  $\{2\}$ . In cases 3) and 4), an external force of 5N and 0.2Nm is applied to  $\{E\}$  with respect to  $\{I\}$ , with 3) having the nominal measurement noise, and 4) having twice the measurement noise. In all four cases, the UAM is commanded to maintain the end-effector at its initial pose. All applied forces and torques are applied as a step at t=1s, and each case is simulated for 15 seconds.

The gains used for control and estimation are shown in Table 2. The gains for the acceleration-based, momentum-based, and hybrid observers are selected so that the wrench estimates settle within 10% of the actual external wrench between t = 3.5s and t = 4s. The EKF process noise covariance matrix is set assuming no process noise in  $\xi$  and  $\dot{\xi}$ , and the remaining diagonal elements are tuned so that the EKF-based wrench estimates settle within 10% of the actual external wrench before t = 4s.

## A. Case 1—Joint-Space, Nominal Measurement Noise

Figures 2, 3, and 4 show direct comparisons between the applied wrench and estimated wrench for Case 1. The plots show the force estimates along the  $p_B$  with respect to  $\{I\}$ , torques about the  $\{B\}$  axes, and the torques about the q joints. Torques about the  $\{B\}$  axes are shown instead of the torques about the  $\varphi_B$  axes for clarity, since the external torque being applied to  $\varphi_B$  varies as  $\varphi_B$  varies. Figure 2 shows results for the entire simulation, and Fig. 3 emphasizes the steady-state results between t = 4s and t = 5s, and Fig. 4 shows the results between t = 14s and t = 15s. The last figure is included to make it easier to distinguish between the noisy estimates.

These plots show that the acceleration-based, momentum-based, and hybrid observers do settle within 10% of the applied wrench within 3s of wrench application. None of these estimates have any overshoot, due to their low gains. From inspection, we can see that the EKF-based observer has comparatively greater noise reduction in the  $\widehat{w}_{e,f}$ ,  $\widehat{w}_{e,\tau_y}$ , and  $\widehat{w}_{e,\tau_z}$  estimates, and less noise reduction everywhere else. For the force estimates, we see that the hybrid and acceleration-based estimates do not actually stabilize around the external force; instead, they sit below the external force. This is caused by the accumulation of error when integrating the discrete signals used for simulation and estimation. Additionally, the acceleration-based and hybrid observers have identical estimates. A related phenomenon is seen in torque estimates about the  $\{B\}$  axes and q joints, where the momentum-based and hybrid wrench observers have identical estimates. This is because the hybrid wrench observer is using the acceleration-based wrench estimation algorithm for force estimation, and the momentum-based algorithm for torque estimation, as can be seen in (24).

Figures 5, 6, and 7 show the root-mean-square error (RMSE) using a 100 sample sliding window for Case 1. Error is defined as the difference between the applied wrench and the estimated wrench, and is denoted as  $\widetilde{\cdot}$ . The error is close to zero between t=0s and t=1s, before growing due to the applied wrench. The estimates settle by t=4s. By looking at Fig. 7, we see that the EKF-based wrench observer has comparatively better estimates for  $w_{e,f}, w_{e,\tau_y}$ , and  $w_{e,\tau_z}$ , and worse estimates everywhere else. Notably, the EKF-based wrench observer is best at removing noise from signals that have the most noise, and worse at removing noise that have little noise. This can be seen in Fig. 7, where the magnitude of  $\widetilde{w}_{e,f_x}$ ,  $\widetilde{w}_{e,f_y}$ ,  $\widetilde{w}_{e,f_z}$ ,  $\widetilde{w}_{e,\tau_y}$ , and  $\widetilde{w}_{e,\tau_z}$  are almost a magnitude larger than  $\widetilde{w}_{e,\tau_x}$ ,  $\widetilde{w}_{e,q_q}$ , and  $\widetilde{w}_{e,q_2}$ .

By looking at the mean of  $w_{e,f_x}$ ,  $w_{e,f_y}$ , and  $w_{e,f_z}$ , we also see that the EKF-based observer does not contain the steady-state error that occurs in the acceleration-based and hybrid observers. A comparison between the observers for these estimates is shown in Table 5.

From Case 1, we can see that the EKF-based wrench observer, compared to the other observers, excels at minimizing noise-based error for signals that have large measurement noise relative to other signals, with the drawback that those other signals errors do not benefit from the EKF-based observer. Additionally, the EKF-based observer does not have

Table 5 Comparison of mean force (N) estimates and their percent errors compared to the applied force between t = 10s and t = 15s for Case 1.

	Acceleration		Momentum		Hybrid		EKF	
	$\widehat{w}$	₩%	$\widehat{w}$	₩%	$\widehat{w}$	₩%	$\widehat{w}$	₩%
$w_{e,f_x}$	4.831	-3.384	4.946	-1.078	4.831	-3.384	5.002	0.046
$w_{e,f_y}$	4.848	-3.034	4.960	-0.802	4.848	-3.034	5.004	0.086
$w_{e,f_z}$	4.815	-3.698	4.957	-0.854	4.815	-3.698	5.004	0.088

Table 6 Comparison of mean force (N) estimates and their percent errors compared to the applied force between t = 10s and t = 15s for Case 2.

	Acceleration		Momentum		Hybrid		EKF	
	$\widehat{w}$	₩%	$\widehat{w}$	₩%	$\widehat{w}$	₩%	$\widehat{w}$	~%
$w_{e,f_x}$	4.440	-11.194	4.893	-2.142	4.440	-11.194	5.016	0.322
$w_{e,f_y}$	4.501	-9.988	4.921	-1.590	4.501	-9.988	5.020	0.400
$w_{e,f_z}$	4.3528	-12.744	4.915	-1.696	4.363	-12.744	5.025	0.504

drift error when estimating external forces, as seen with the acceleration-based and hybrid observers.

# B. Case 2—Joint-Space, Doubled Measurement Noise

Case 2 has many similarities to Case 1, with the primary difference being worse estimates for all observers due to the increased noise. Figures 8, 9, and 10 show larger errors than in Case 1. In the case of force estimates, the acceleration-based and hybrid estimates have a larger steady-state errors than before, which can be seen when comparing Tables 5 and 6.

Figures 11, 12, and 13 show the RMSE of Case 2, using a sliding window of 100 samples. When looking at the final steady state with Fig. 13, we see that the force estimate RMSE by the acceleration-based observer tripled compared to Case 1, and the torque estimates are doubled. The momentum-based observer RMSE doubles in every case except for  $w_{e,q_1}$ , where it only increases by a factor of 1.5. The hybrid RMSE has the same tripling in RMSE for force estimation, and doubling RMSE for torque estimation, except for  $w_{e,q_1}$ . The EKF-based RMSE doubles between Case 1 and Case 2.

By doubling the noise in the measurement signals, we see that the acceleration-based observer is the most negatively impacted, followed by the hybrid observer, the EKF-based observer, then the momentum-based observer. Similar to Case 1, we still see that the EKF-based wrench observer excels at minimizing the largest noise-based errors compared to the other observers, but does not reduce the noise in signals with small noise. Additionally, the EKF-based observer does not have drift error when estimating external forces, as seen with the acceleration-based and hybrid observer.

### C. Case 3—Operational Space, Nominal Measurement Noise

Figures 14, 15, and 16 show the direct comparisons between the applied wrench on the end-effector and the estimated wrench in operational space for Case 3. Figure 14 shows the results for the entire simulation, Fig. 15 emphasizes the steady-state results between t = 4s and t = 15s, and Fig. 16 shows the results between t = 14s and t = 15s. The last figure is included to make it easier to distinguish between the noisy estimates.

For force estimates, we see that the EKF-based estimates consistently overshoot the applied wrench by 5%, while all other observers do not overshoot. For torque estimate, the EKF-based estimates have overshoots and an undershoot exceeding 300% between t = 1s and t = 4s. The torque estimates provided by the other observers are dominated by noise, making it difficult to distinguish the actual external torque. An average of the torque estimates between t = 10s and t = 15s is shown in Table 7, showing that the average estimate across 5 seconds is within 20% for all observers. This indicates that a low-pass filter may be added to these observers at the cost of significant lag. While noise does dominate the signal for the acceleration-based, momentum-based, and hybrid observer, this does not necessarily mean that accurate torque estimates without a low-pass filter are impossible in general. In this work, a combination of the underactuated UAM platform and a basic motion controller limits the amount of torque able to be applied to the

Table 7 Comparison of mean torque (Nm) estimates and their percent errors compared to the applied torque between t = 10s and t = 15s for Case 3.

	Acceleration		Momentum		Hybrid		EKF	
	$\widehat{ au}$	$\widetilde{ au}\%$	$\widehat{ au}$	$\widetilde{ au}\%$	$\widehat{ au}$	~~~~~~~~~~~~~~~~~~~~~~~~~~~~~~~~~~~~~~	$\widehat{ au}$	$\widetilde{ au}\%$
$\tau_x$	0.206	2.850	0.206	2.800	0.209	4.350	0.207	3.300
$ au_y$	0.181	-9.450	0.184	-8.050	0.162	-18.850	0.193	-3.400
$ au_z$	0.208	4.000	0.206	2.800	0.228	14.000	0.187	-6.600

Table 8 Comparison of mean torque (Nm) estimates and their percent errors compared to the applied torque between t = 10s and t = 15s for Case 4.

	Acceleration		Momentum		Hybrid		EKF	
	$\widehat{ au}$	~~~~~~~~~~~~~~~~~~~~~~~~~~~~~~~~~~~~~~						
$ au_{\chi}$	0.216	7.900	0.216	7.750	0.239	19.250	0.213	6.650
$ au_y$	0.155	-22.500	0.164	-17.950	0.057	-71.300	0.183	-8.350
$ au_{z}$	0.234	17.150	0.227	13.300	0.310	55.200	0.173	-13.450

end-effector before the UAM goes unstable. If a fully actuated platform or robust motion controller are used instead, larger torques may be applied to the end-effector, and the ratio of noise to signal can be favorable for torque estimates. Regardless of the limitations of the current platform, the EKF-based torque estimates may be usable, as seen in Fig. 17, 18, and 19.

By looking at the RMSE shown in Fig. 17, 18, and 19, the steady-state wrench estimate by the EKF is better than the other observers, with only the momentum-based observer occasionally having lower RMSE for the force estimates.

# D. Case 4—Operational Space, Doubled Measurement Noise

Case 4 has many similarities to Case 3, with the primary difference being the worsened estimates for all observers due to the increased measurement noise. Figures 20, 21, and 22 show larger errors than in Case 3.

By looking at the steady-state RMSE shown in Fig. 23, 24, and 25, and comparing them against Case 3, we see that the RMSE doubles for the momentum- and EKF-based observer, while the RMSE for the other observers triples or quadruples. This indicates that the acceleration-based and hybrid observers are more sensitive to additional noise compared to the momentum- or EKF-based observers.

In both Case 3 and 4, we see that the EKF-based observer is the least noisy and most accurate, showing that it is effective in estimating external wrenches under steady-state conditions.

# VII. Conclusion

In this paper, acceleration-based, momentum-based, hybrid, and EKF-based wrench observers are presented, and their performance in estimating external wrenches is shown in both joint-space and operational space. We show that in joint-space, the EKF-based observer is effective in reducing noise in signals which contained the most noise when compared to acceleration-based, momentum-based, and hybrid wrench observers. We also show that the acceleration-based and hybrid observers are subject to drift while reaching steady state, causing a steady-state error. In operational space, we show that the EKF-based observer is superior in reducing noise and obtaining the most accurate wrench estimates out of all the observers.

Future work will focus on developing a method to obtain time-varying measurement covariance matrix so that the EKF-based observer can make the tradeoff in real-time between fast response during transient periods, and accuracy during steady state. Furthermore, this algorithm will be validated on hardware to demonstrate real-world viability.

# References

- [1] Hamaza, S., Georgilas, I., Fernandez, M., Sanchez, P., Richardson, T., Heredia, G., and Ollero, A., "Sensor Installation and Retrieval Operations Using an Unmanned Aerial Manipulator," *IEEE Robotics and Automation Letters*, Vol. 4, No. 3, 2019, pp. 2793–2800. https://doi.org/10.1109/LRA.2019.2918448, conference Name: IEEE Robotics and Automation Letters.
- [2] Trujillo, M. Á., Martínez-de Dios, J. R., Martín, C., Viguria, A., and Ollero, A., "Novel aerial manipulator for accurate and robust industrial NDT contact inspection: A new tool for the oil and gas inspection industry," *Sensors*, Vol. 19, No. 6, 2019, p. 1305.
- [3] Bodie, K., Brunner, M., Pantic, M., Walser, S., Pfändler, P., Angst, U., Siegwart, R., and Nieto, J., "An omnidirectional aerial manipulation platform for contact-based inspection," *arXiv* preprint arXiv:1905.03502, 2019.
- [4] Tzoumanikas, D., Graule, F., Yan, Q., Shah, D., Popovic, M., and Leutenegger, S., "Aerial manipulation using hybrid force and position nmpc applied to aerial writing," *arXiv preprint arXiv:2006.02116*, 2020.
- [5] De Luca, A., Albu-Schaffer, A., Haddadin, S., and Hirzinger, G., "Collision detection and safe reaction with the DLR-III lightweight manipulator arm," 2006 IEEE/RSJ International Conference on Intelligent Robots and Systems, IEEE, 2006, pp. 1623–1630.
- [6] Van Damme, M., Beyl, P., Vanderborght, B., Grosu, V., Van Ham, R., Vanderniepen, I., Matthys, A., and Lefeber, D., "Estimating robot end-effector force from noisy actuator torque measurements," 2011 IEEE International Conference on Robotics and Automation, IEEE, 2011, pp. 1108–1113.
- [7] Yüksel, B., Secchi, C., Bülthoff, H. H., and Franchi, A., "A nonlinear force observer for quadrotors and application to physical interactive tasks," 2014 IEEE/ASME international conference on advanced intelligent mechatronics, IEEE, 2014, pp. 433–440.
- [8] Yüksel, B., Secchi, C., Bülthoff, H. H., and Franchi, A., "Reshaping the physical properties of a quadrotor through IDA-PBC and its application to aerial physical interaction," 2014 IEEE International Conference on Robotics and Automation (ICRA), IEEE, 2014, pp. 6258–6265.
- [9] Ruggiero, F., Cacace, J., Sadeghian, H., and Lippiello, V., "Impedance control of VToL UAVs with a momentum-based external generalized forces estimator," 2014 IEEE international conference on robotics and automation (ICRA), IEEE, 2014, pp. 2093–2099.

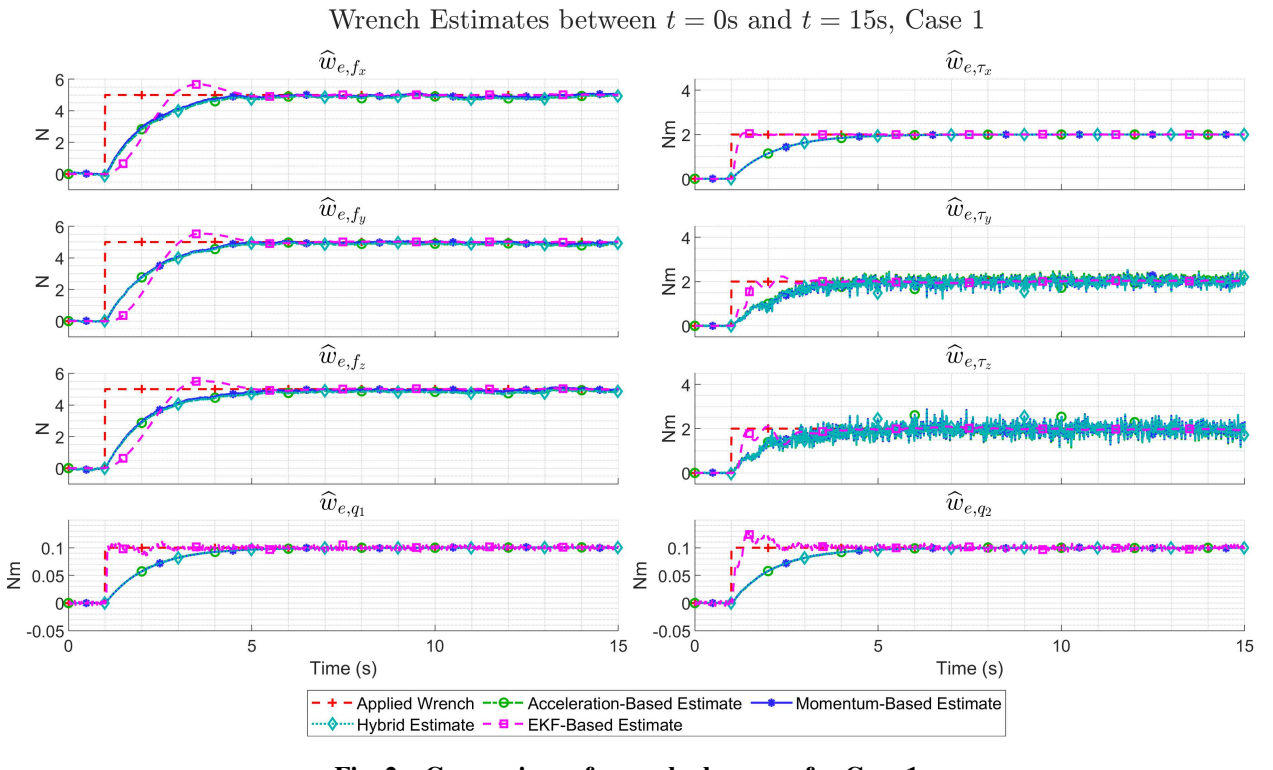


Fig. 2 Comparison of wrench observers for Case 1.

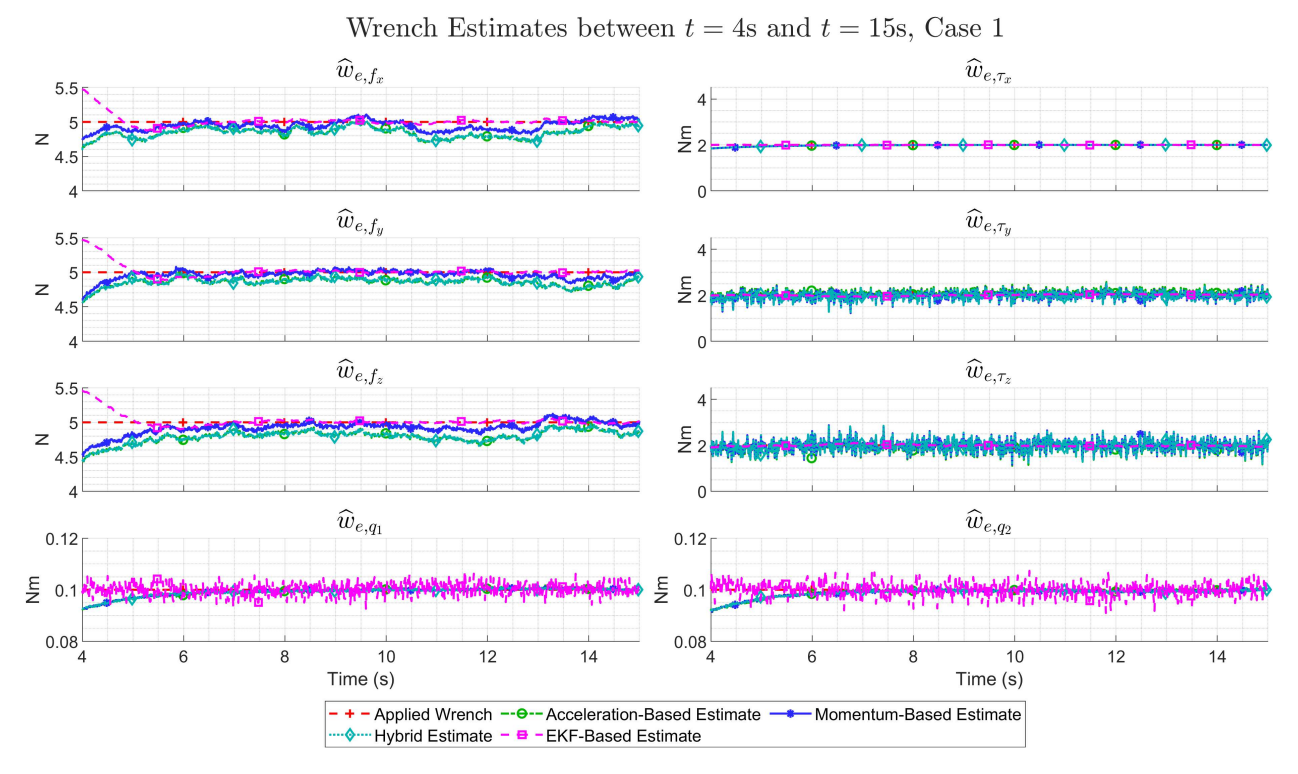


Fig. 3 Comparison of wrench observers for Case 1 between t = 4s and t = 15s.

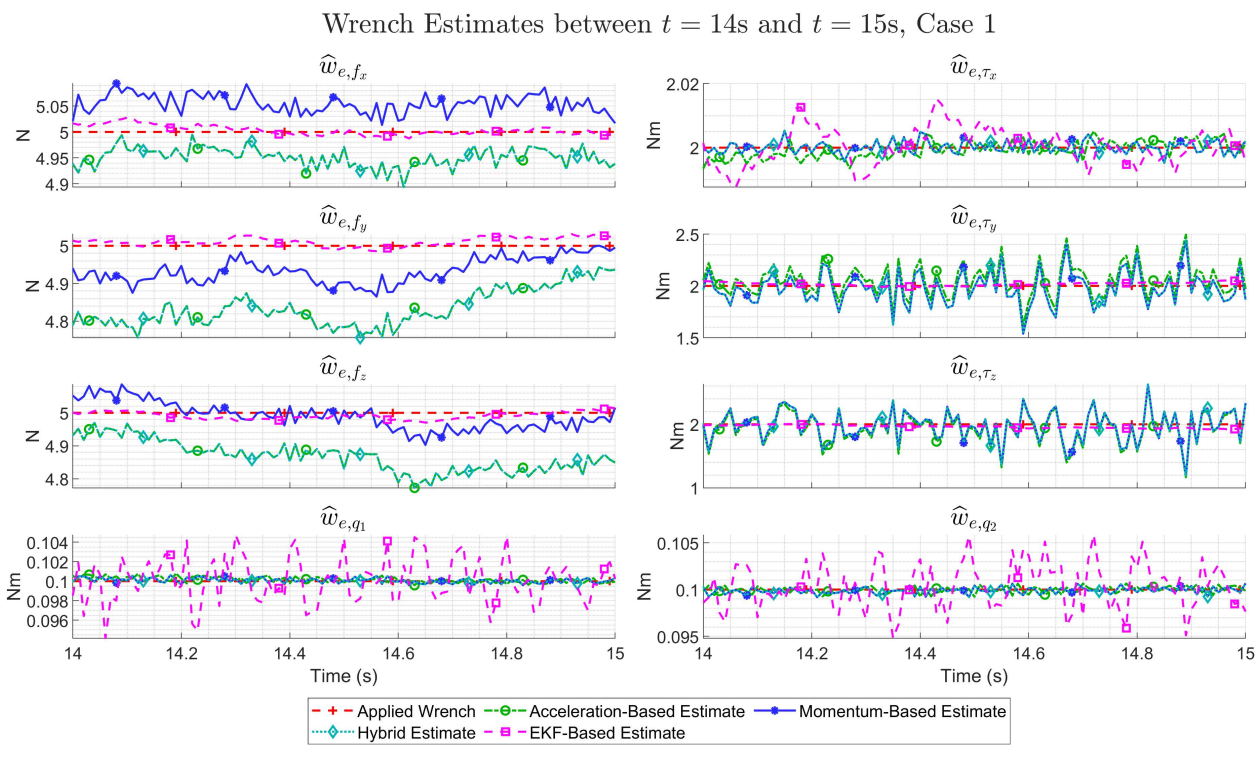


Fig. 4 Comparison of wrench observers for Case 1 between t=14s and t=15s. Note that the y-axis limits are not identical for  $\widehat{w}_{e,\tau}$ , so that differences in estimation can be seen more easily for  $\widehat{w}_{e,\tau_x}$ .

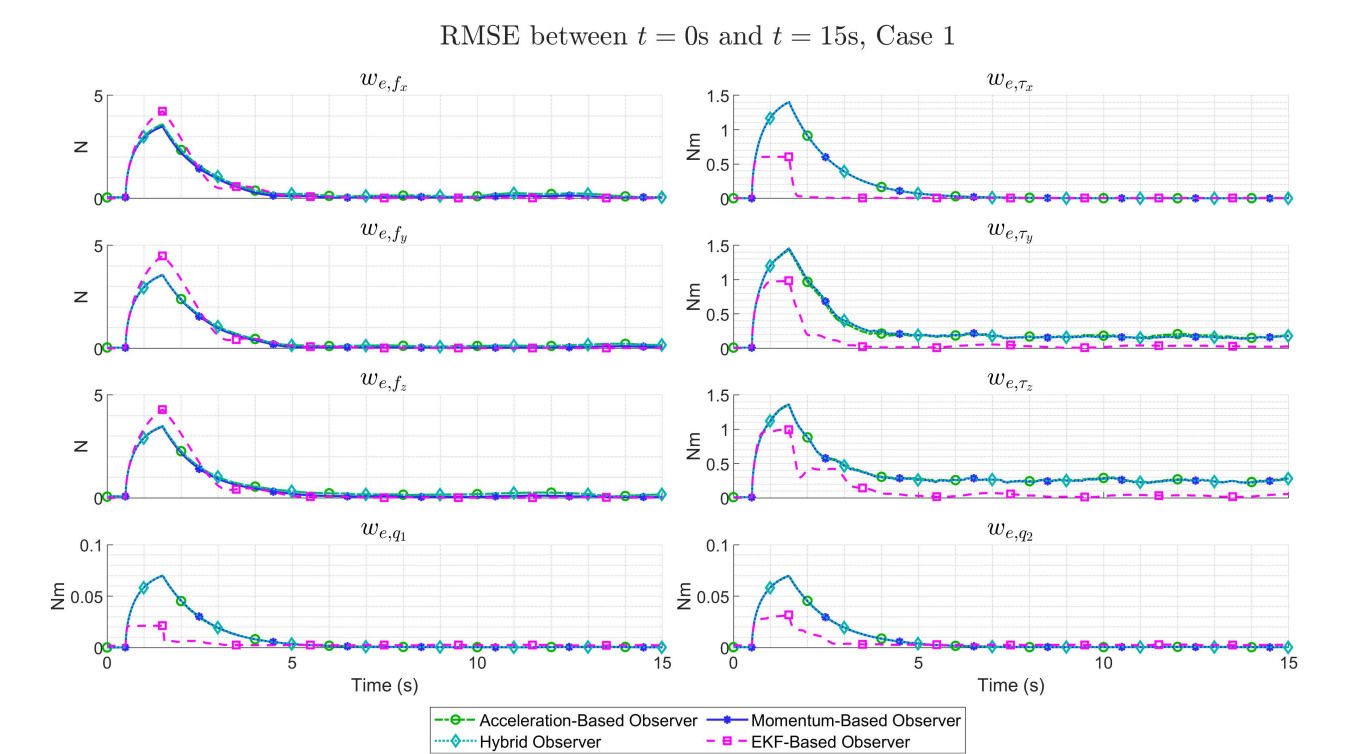


Fig. 5 RMSE using a 100 sample sliding window for Case 1.

··♦···· Hybrid Observer

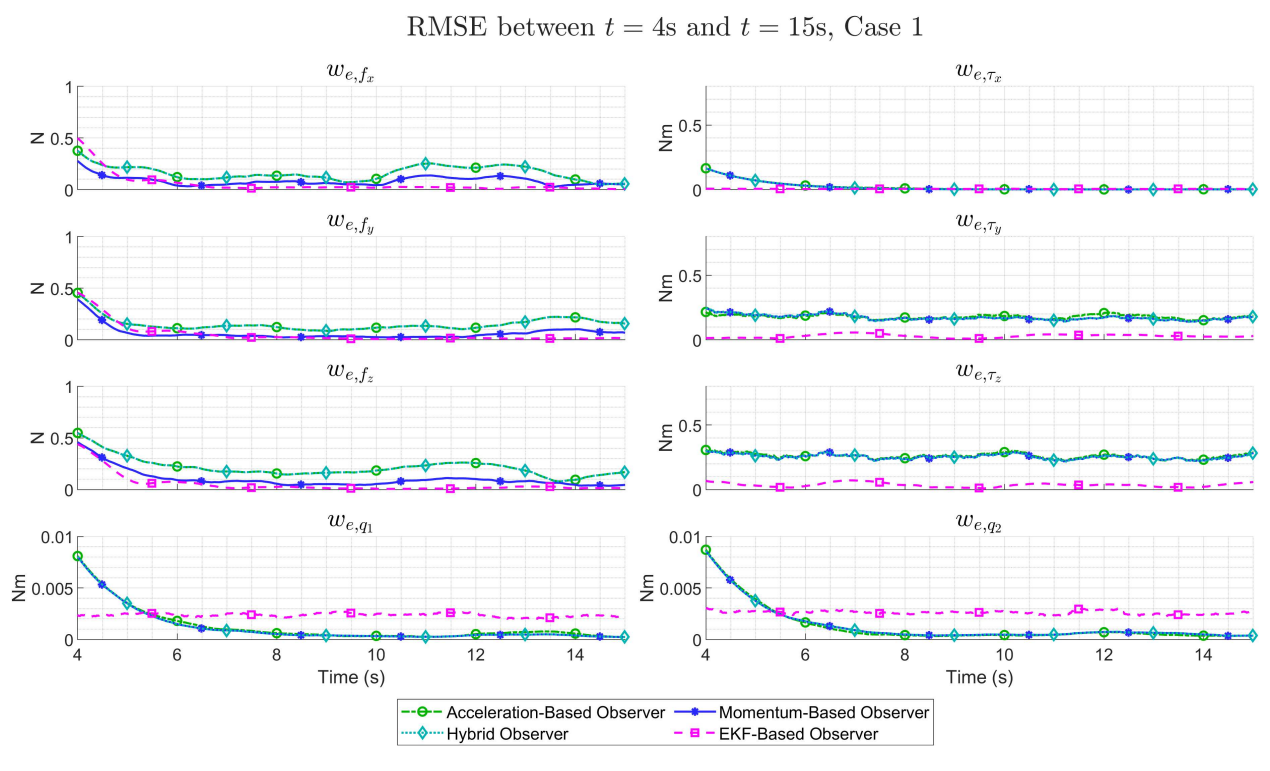


Fig. 6 RMSE using a 100 sample sliding window for Case 1 between t = 4s and t = 15s.

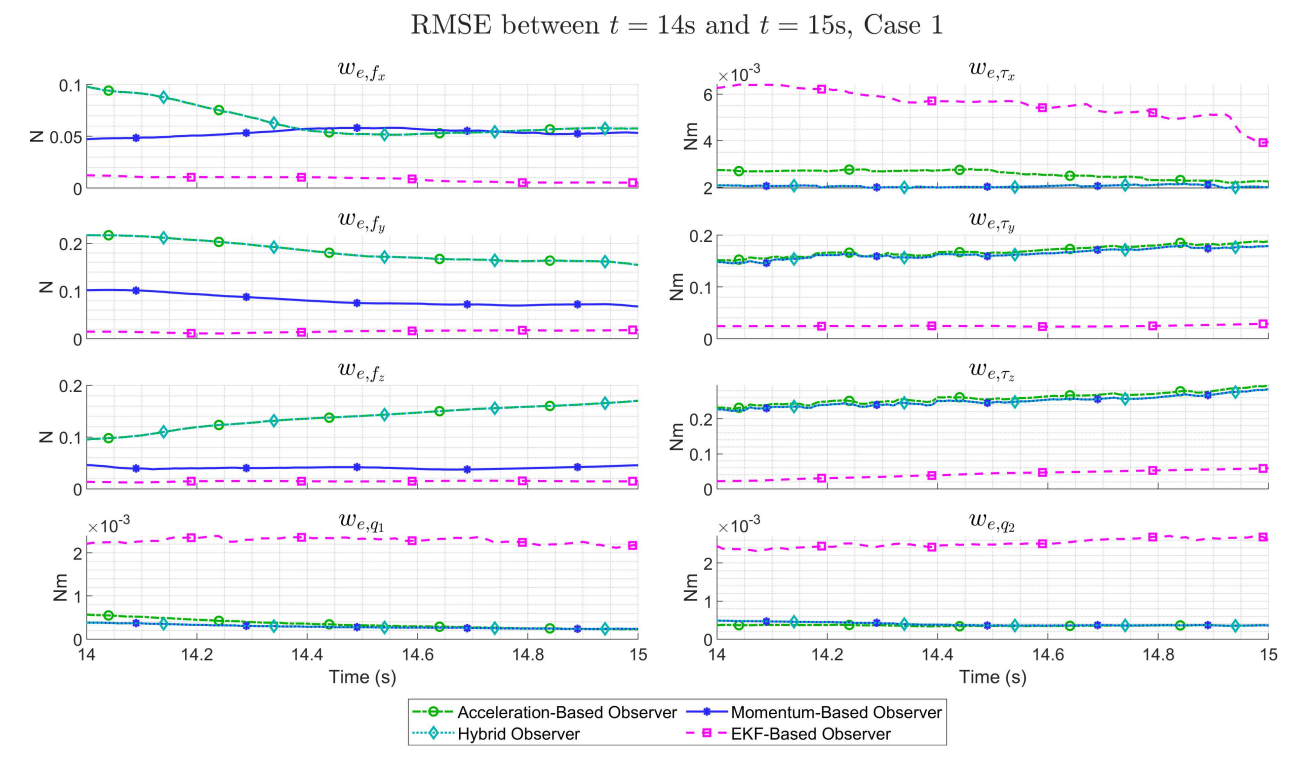


Fig. 7 RMSE using a 100 sample sliding window for Case 1 between t=4s and t=15s. Note that the y-axis limits for  $w_{e,\tau}$  differ significantly, so that  $w_{e,\tau_x}$  can be seen with greater clarity.

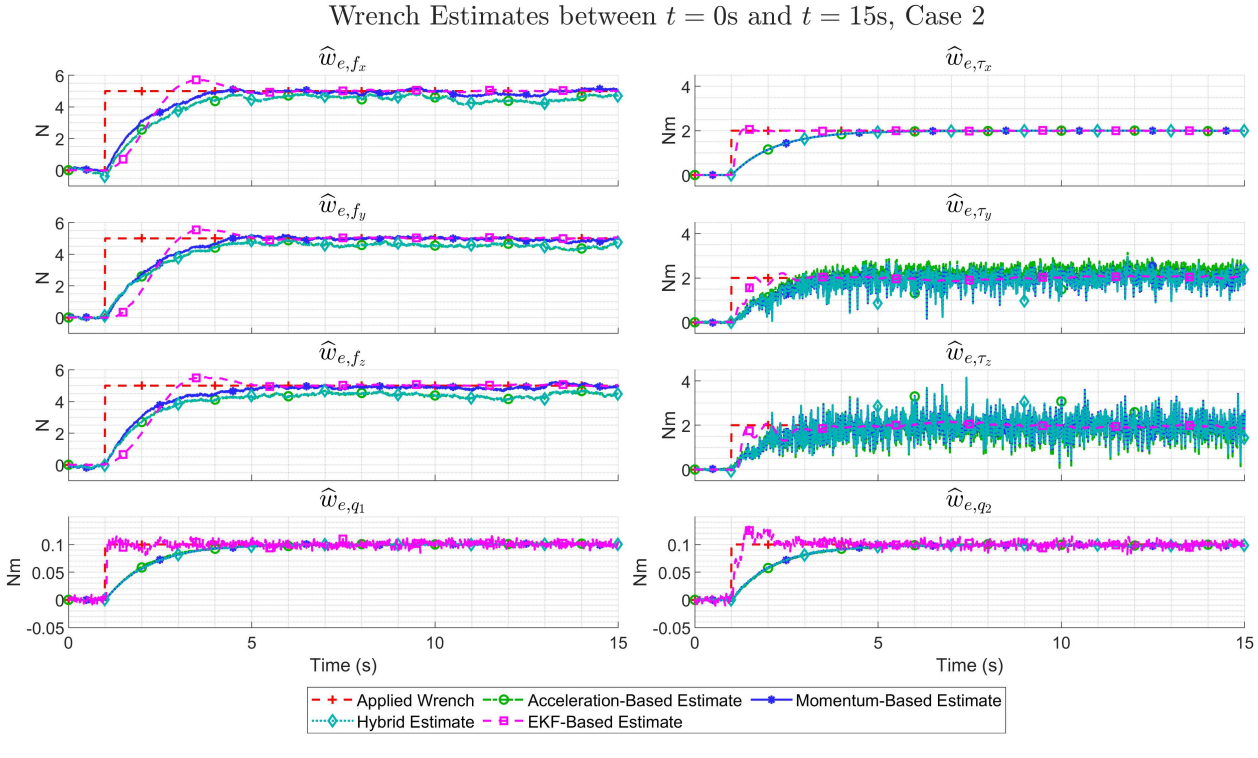


Fig. 8 Comparison of wrench observers for Case 2.

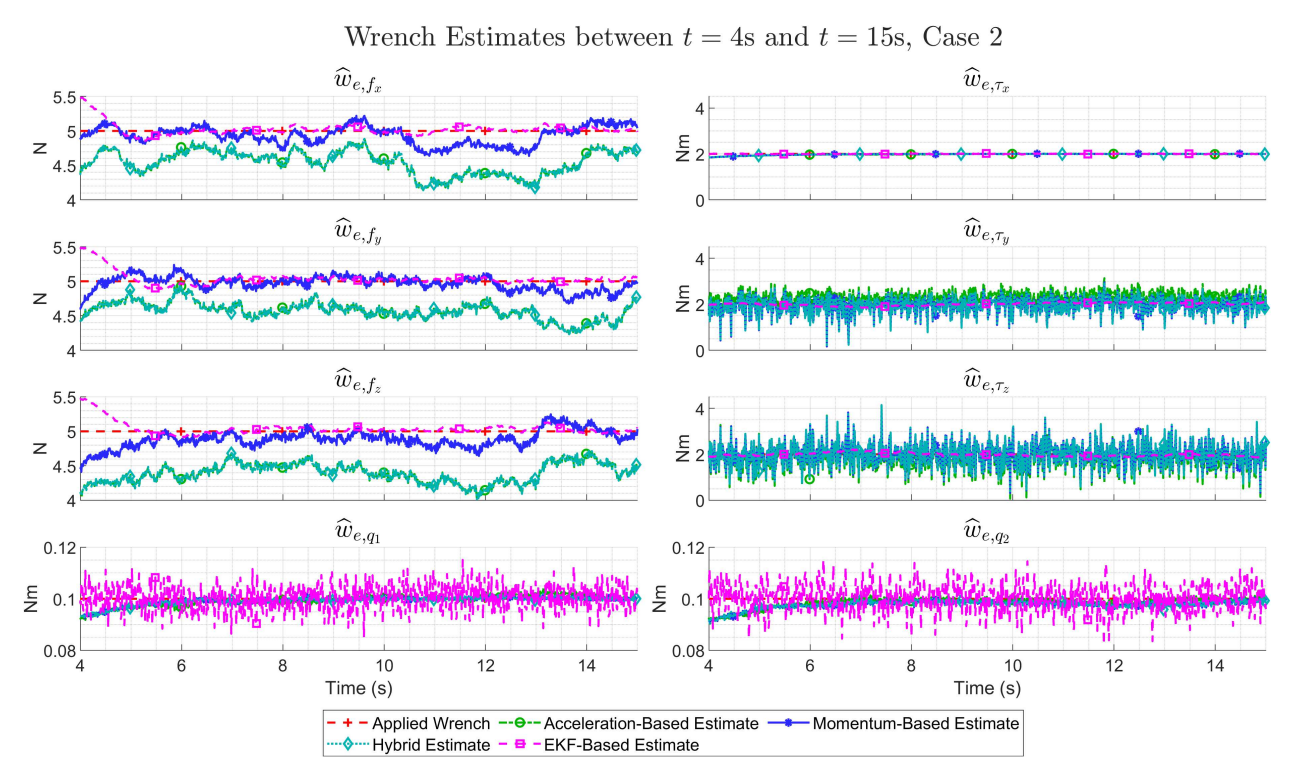


Fig. 9 Comparison of wrench observers for Case 2 between t = 4s and t = 15s.

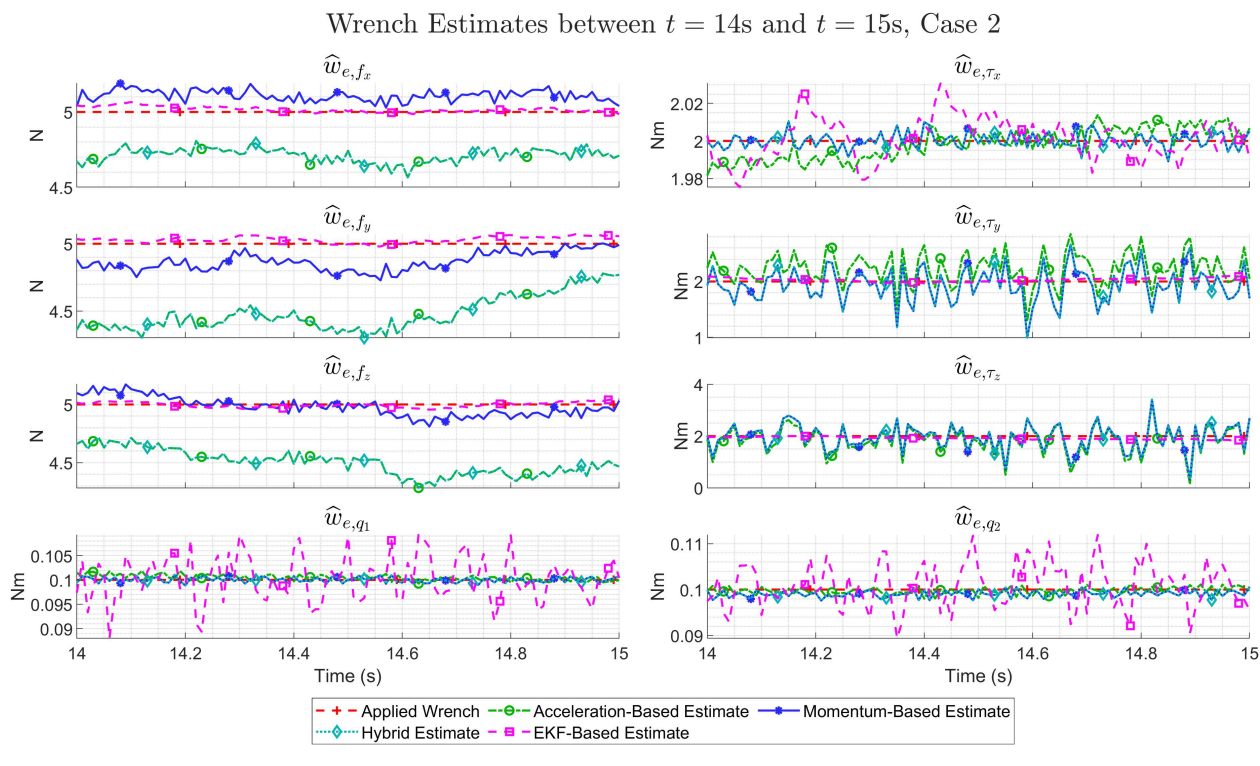


Fig. 10 Comparison of wrench observers for Case 2 between t=14s and t=15s. Note that the y-axis limits are not identical for  $\widehat{w}_{e,\tau}$ , so that differences in estimation can be seen more easily for  $\widehat{w}_{e,\tau_x}$ .

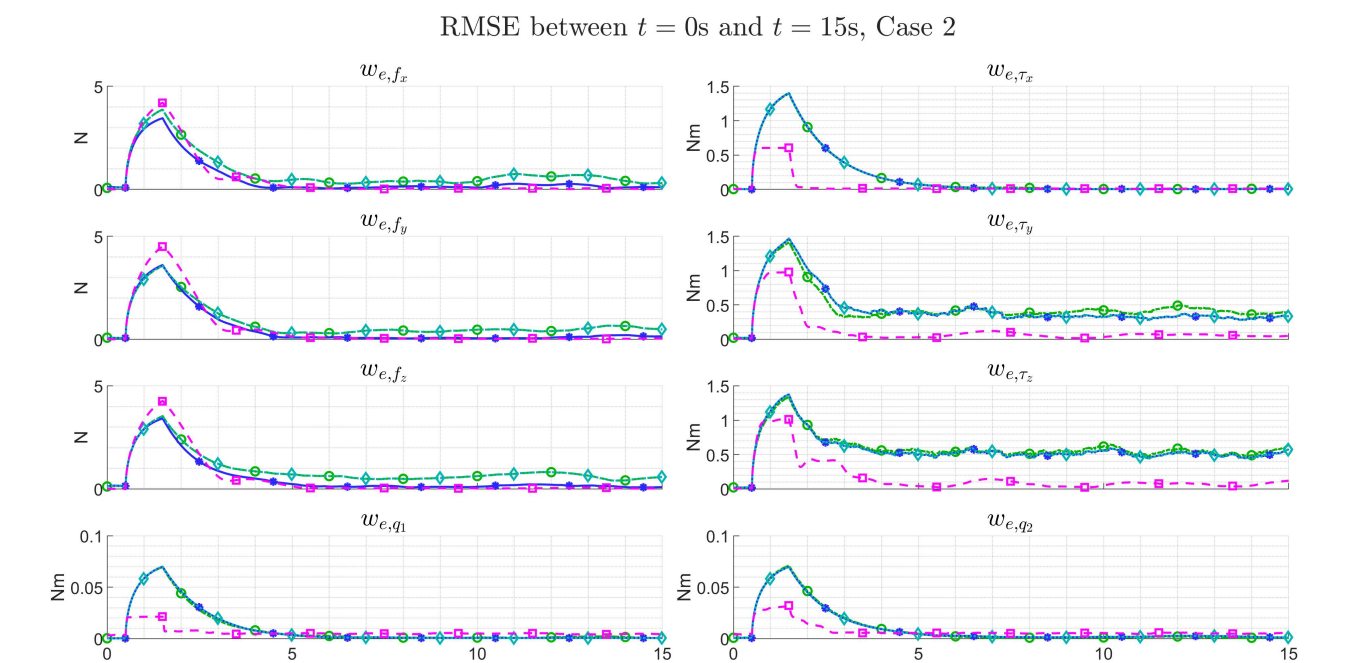


Fig. 11 RMSE using a 100 sample sliding window for Case 2.

---- Acceleration-Based Observer --

Time (s)

− Momentum-Based Observer − EKF-Based Observer

Time (s)

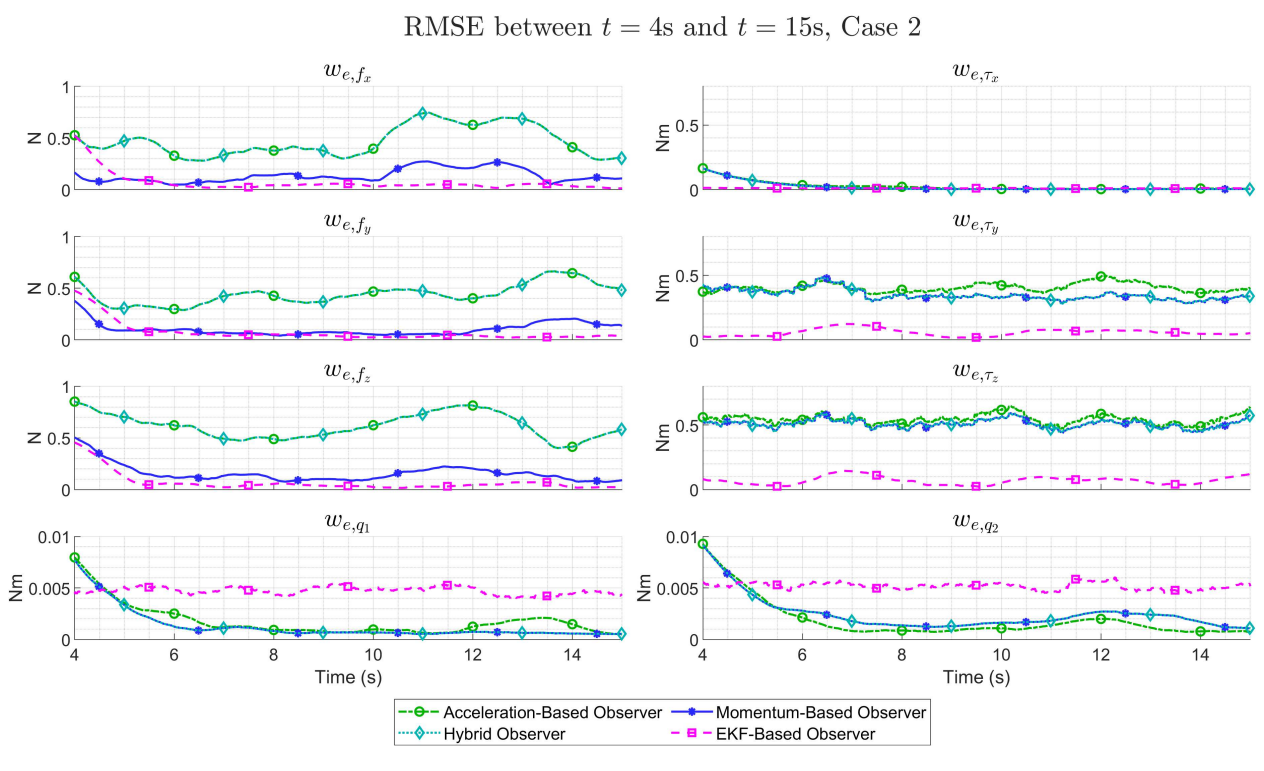


Fig. 12 RMSE using a 100 sample sliding window for Case 2 between t = 4s and t = 15s.

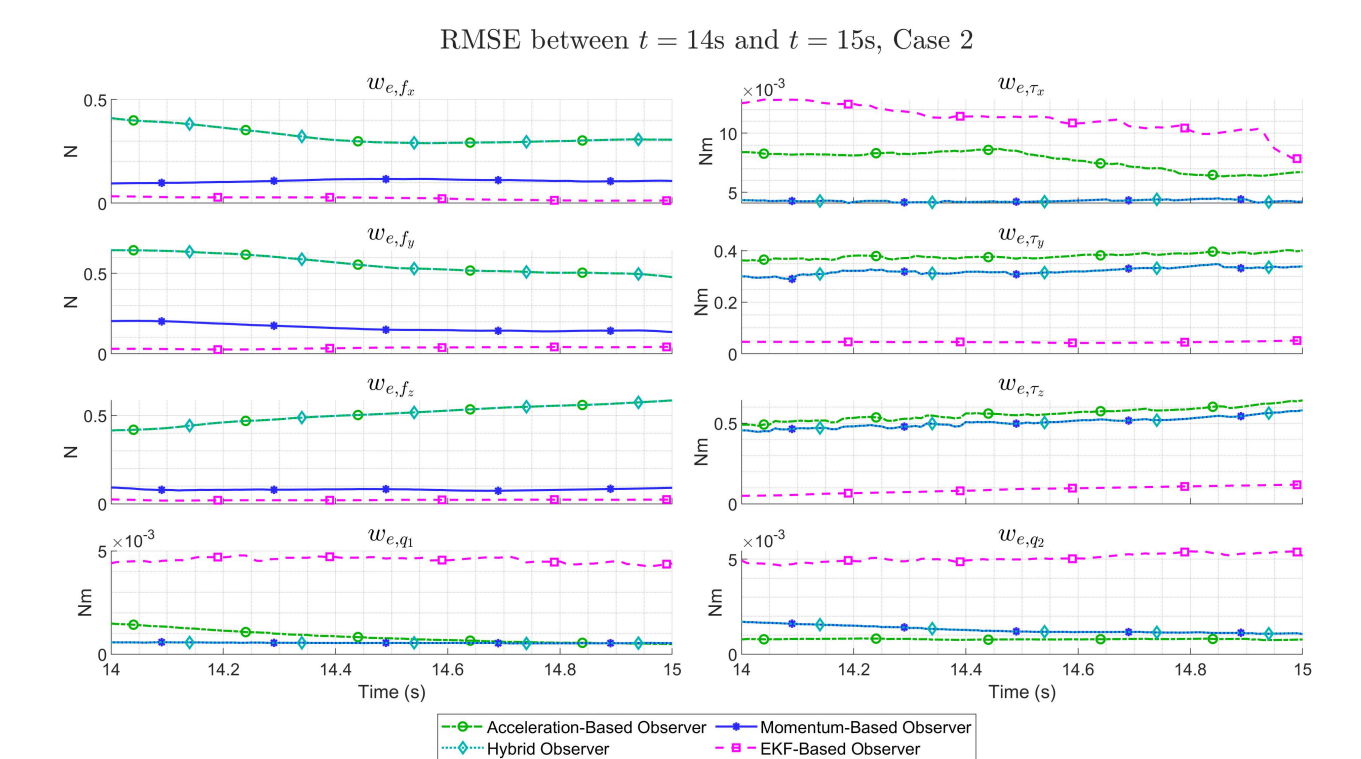


Fig. 13 RMSE using a 100 sample sliding window for Case 2 between t=14s and t=15s. Note that the y-axis limits for  $w_{e,\tau}$  differ significantly, so that  $w_{e,\tau_x}$  can be seen with greater clarity.

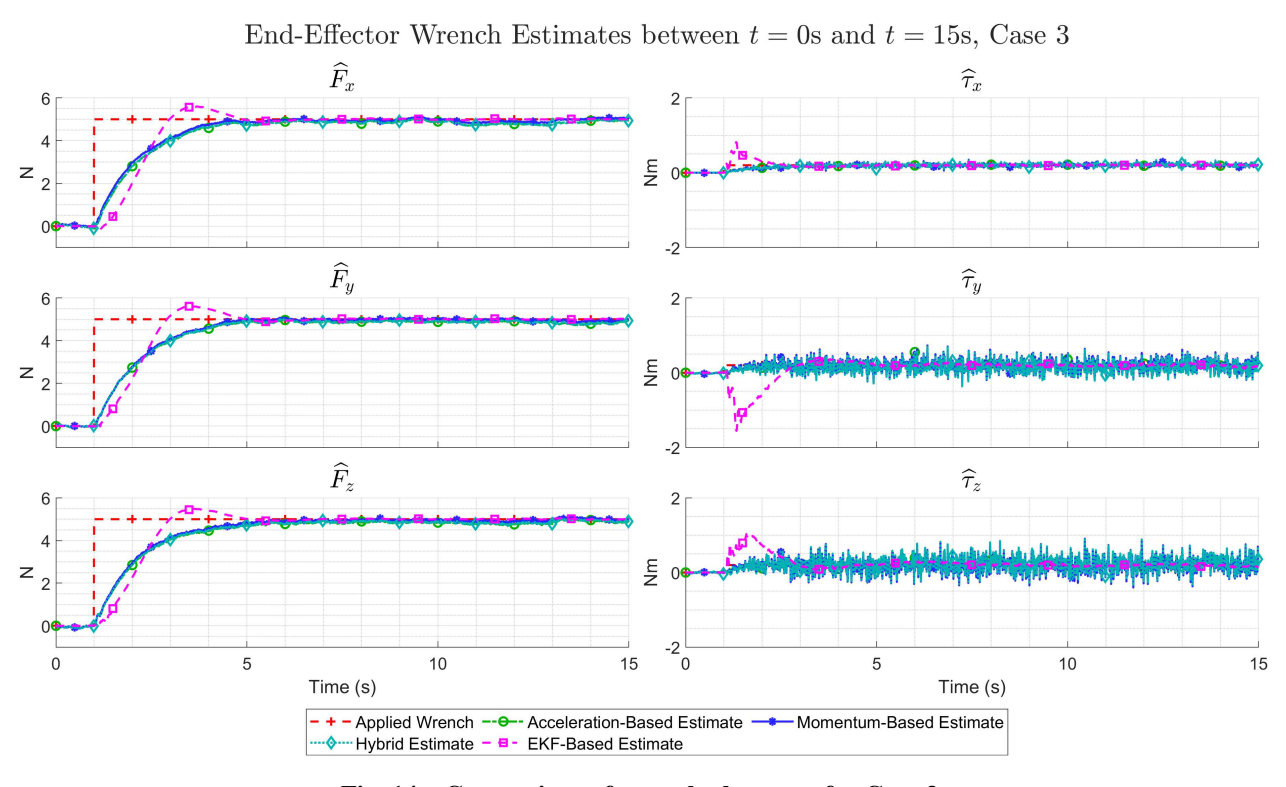


Fig. 14 Comparison of wrench observers for Case 3.

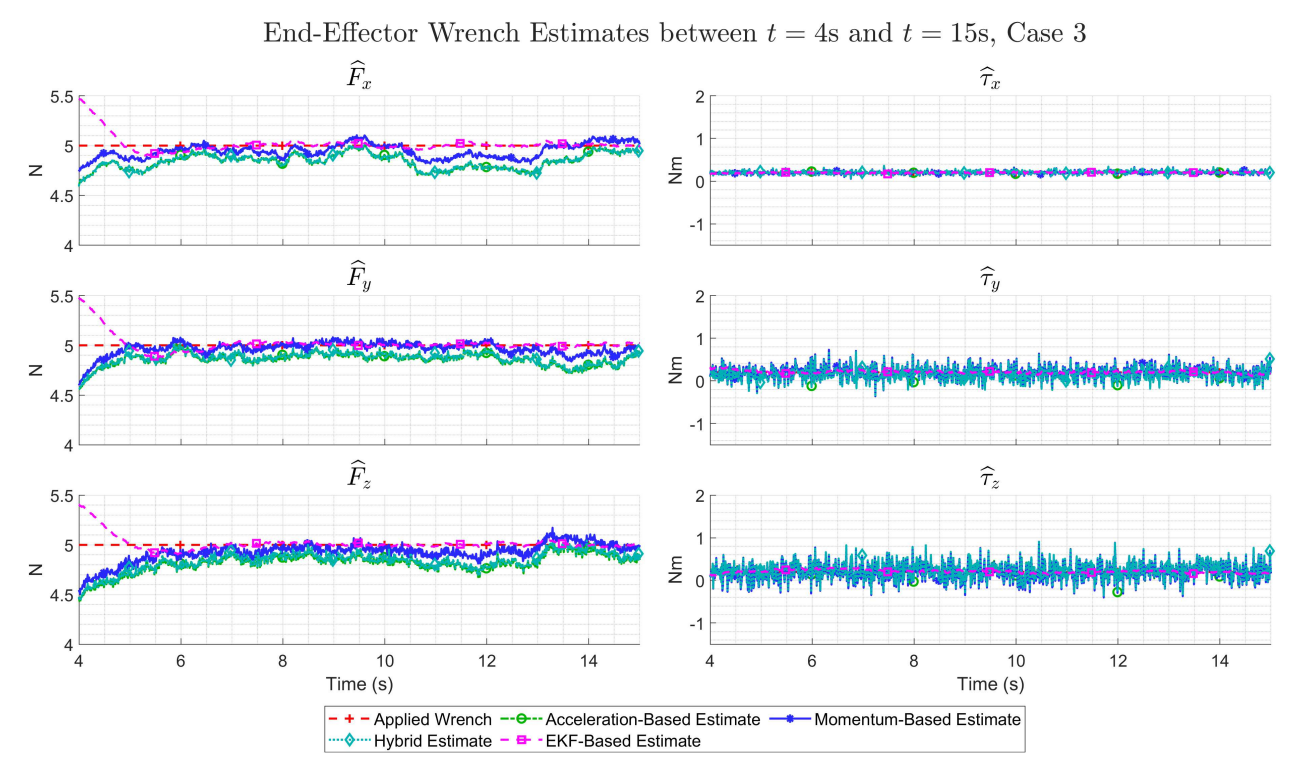


Fig. 15 Comparison of wrench observers for Case 3 between t = 4s and t = 15s.

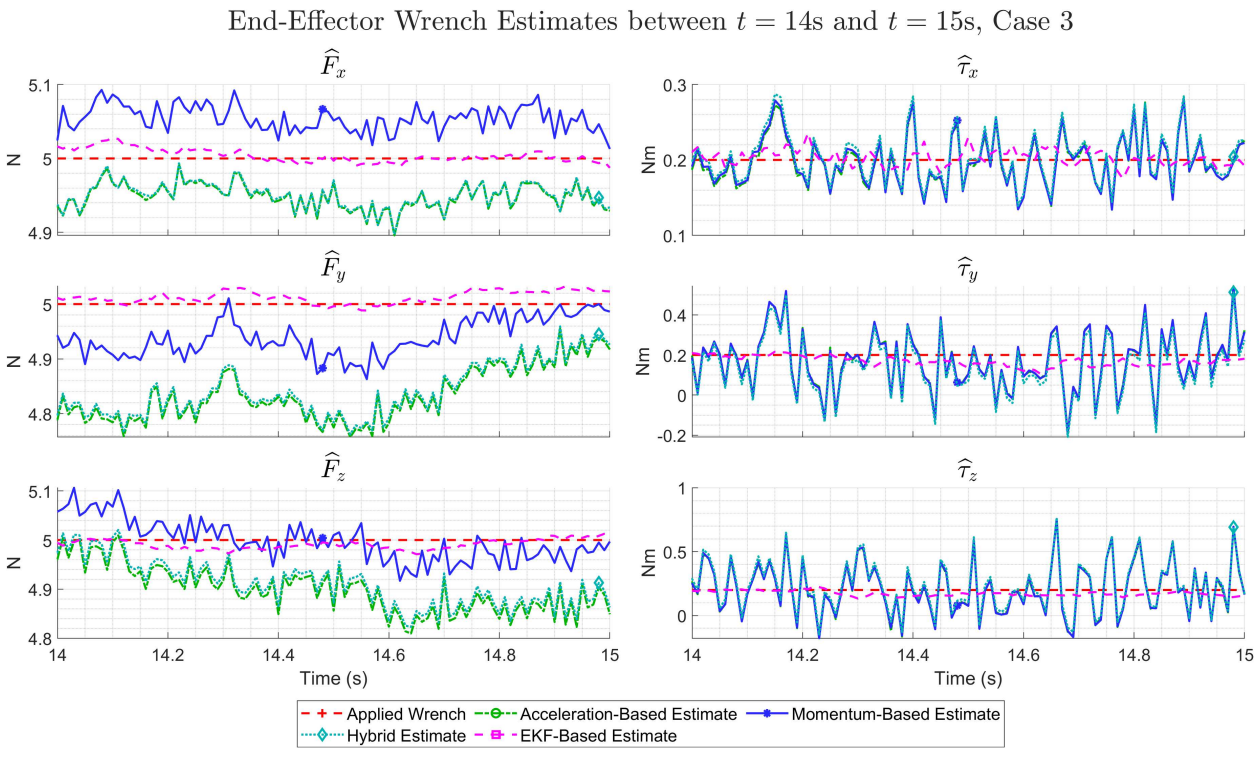


Fig. 16 Comparison of wrench observers for Case 3 between t = 14s and t = 15s. Note that the y-axis limits are not identical, so that differences in estimation can be seen more easily.

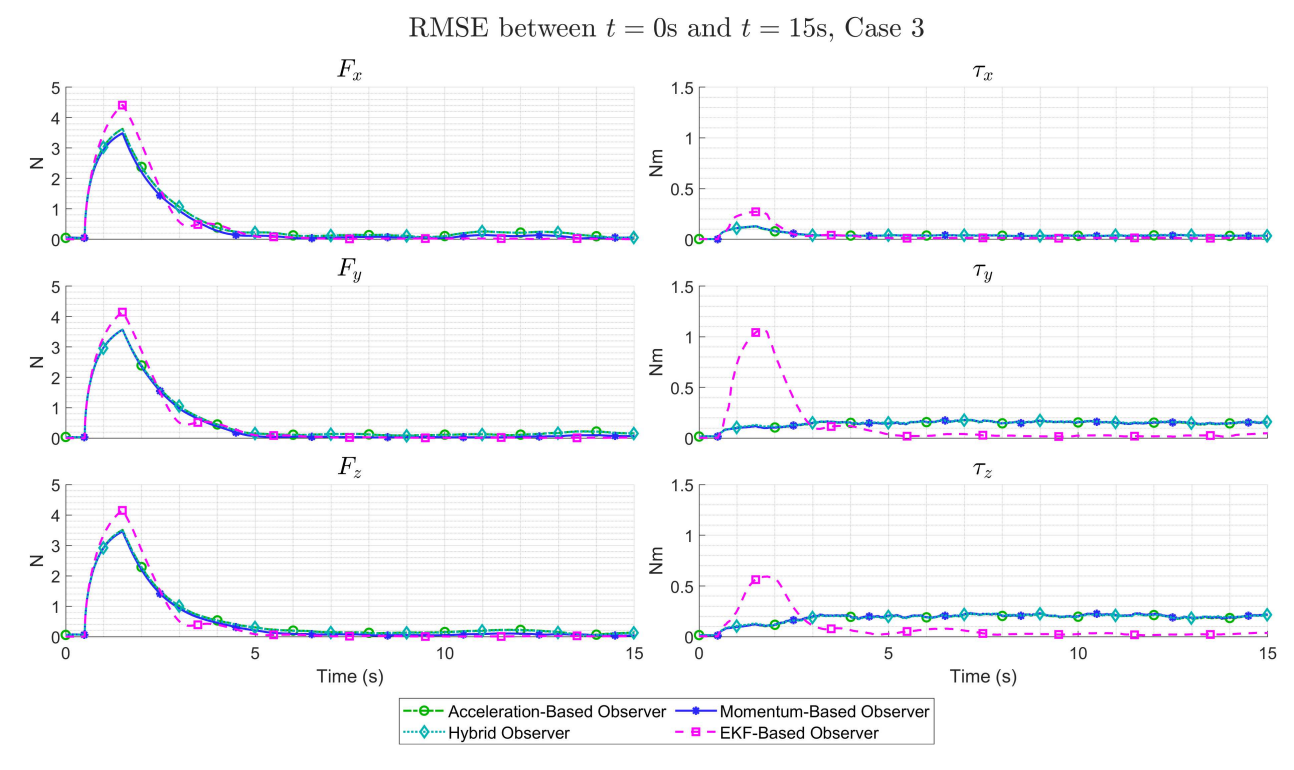


Fig. 17 RMSE using a 100 sample sliding window for Case 3.

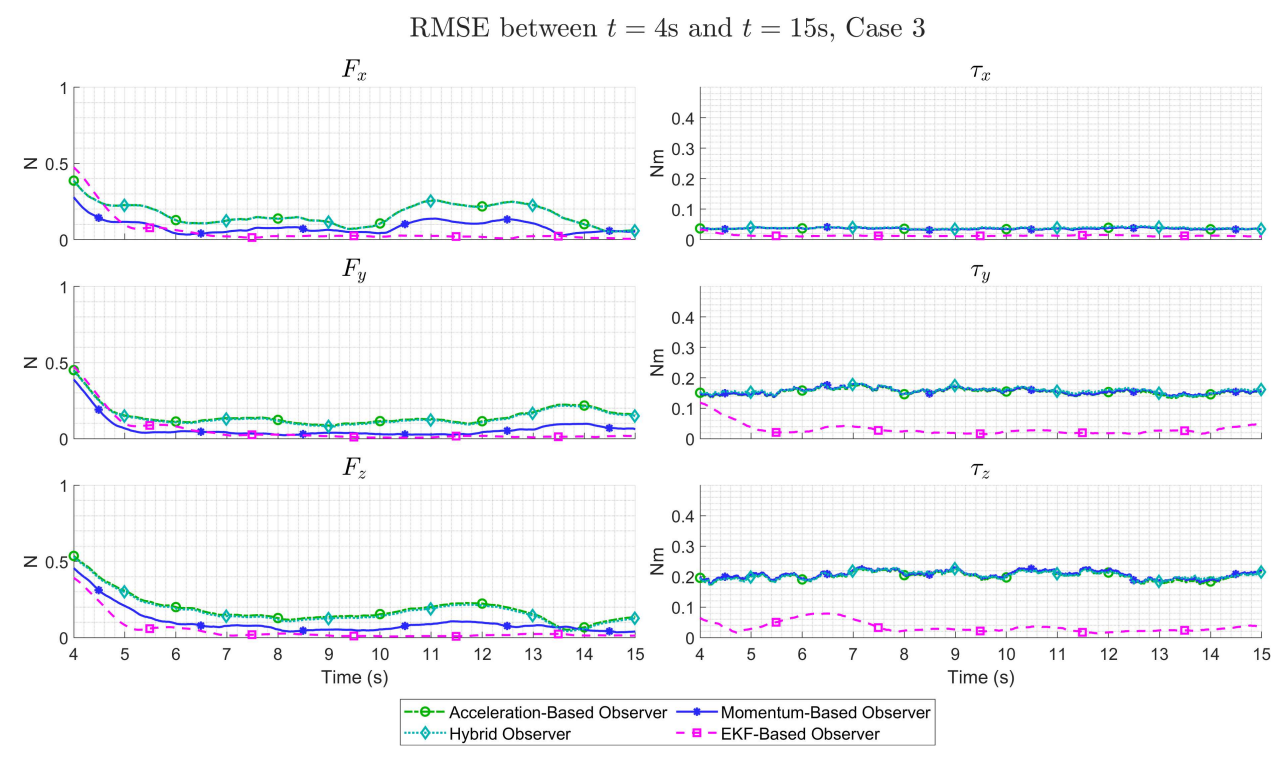


Fig. 18 RMSE using a 100 sample sliding window for Case 3 between t = 4s and t = 15s.

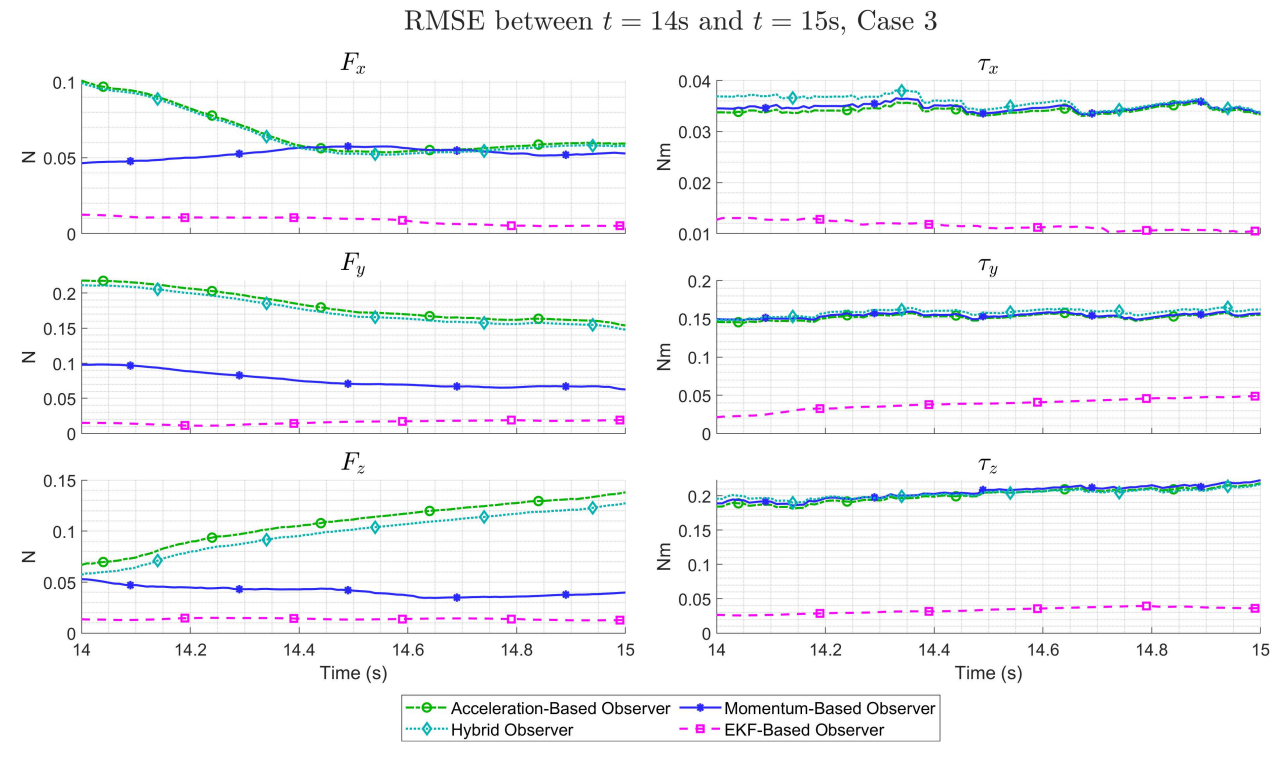


Fig. 19 RMSE using a 100 sample sliding window for Case 3 between t = 14s and t = 15s. Note that the y-axis limits for differ significantly, so that differences in RMSE can be seen with greater clarity.

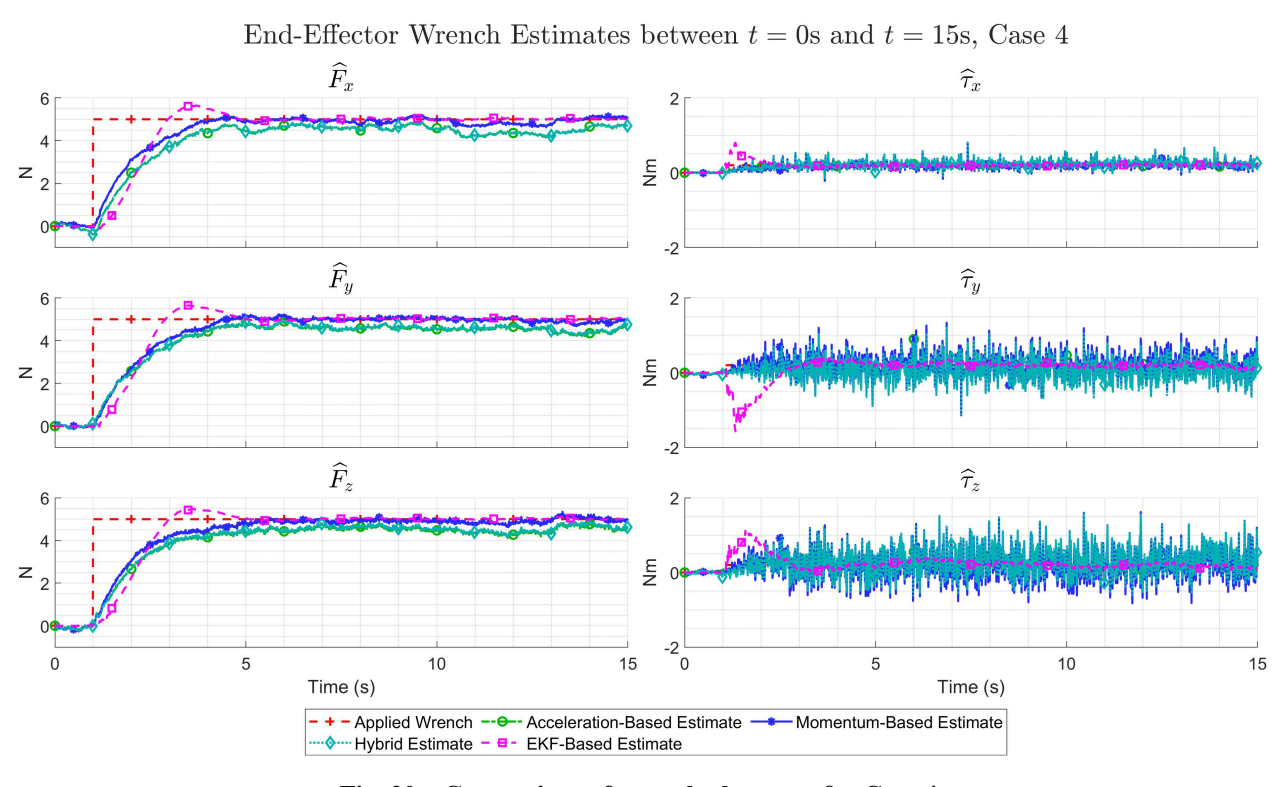


Fig. 20 Comparison of wrench observers for Case 4.

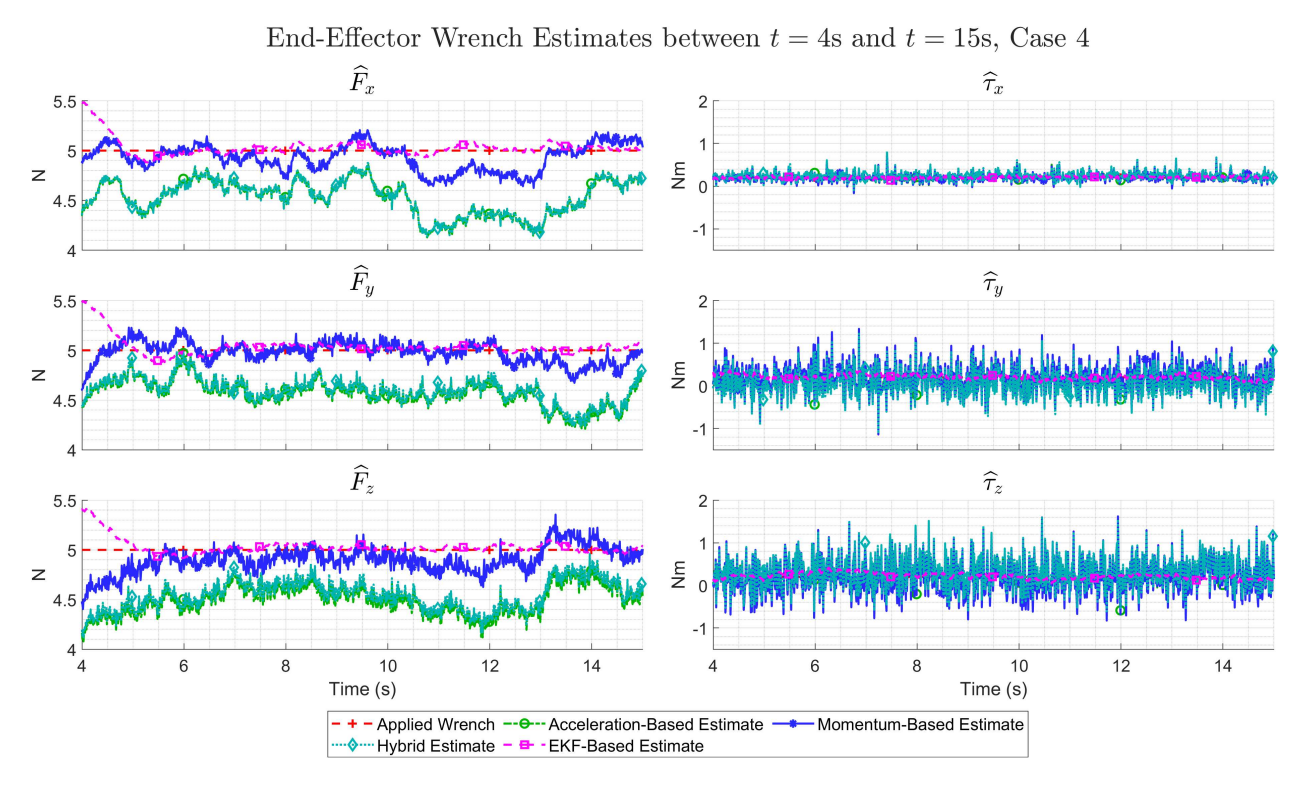


Fig. 21 Comparison of wrench observers for Case 4 between t = 4s and t = 15s.

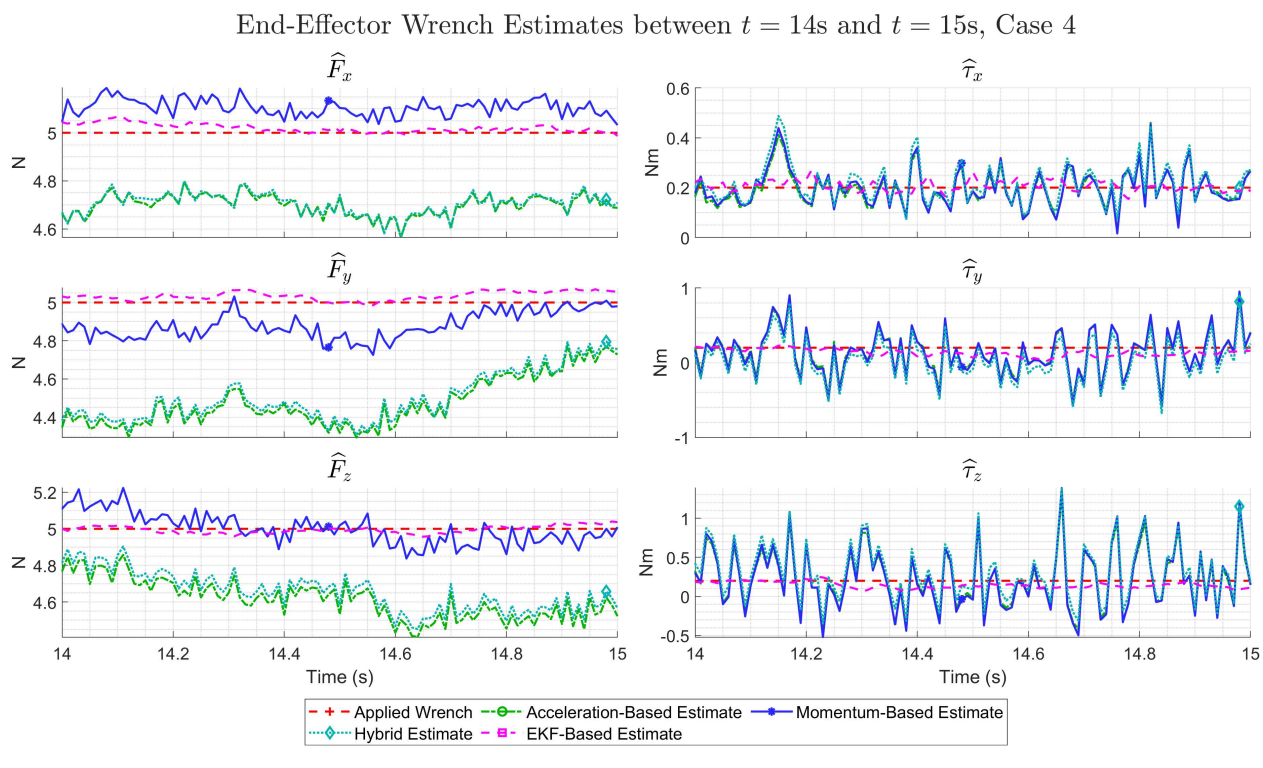


Fig. 22 Comparison of wrench observers for Case 4 between t = 14s and t = 15s. Note that the y-axis limits are not identical, so that differences in estimation can be seen more easily.

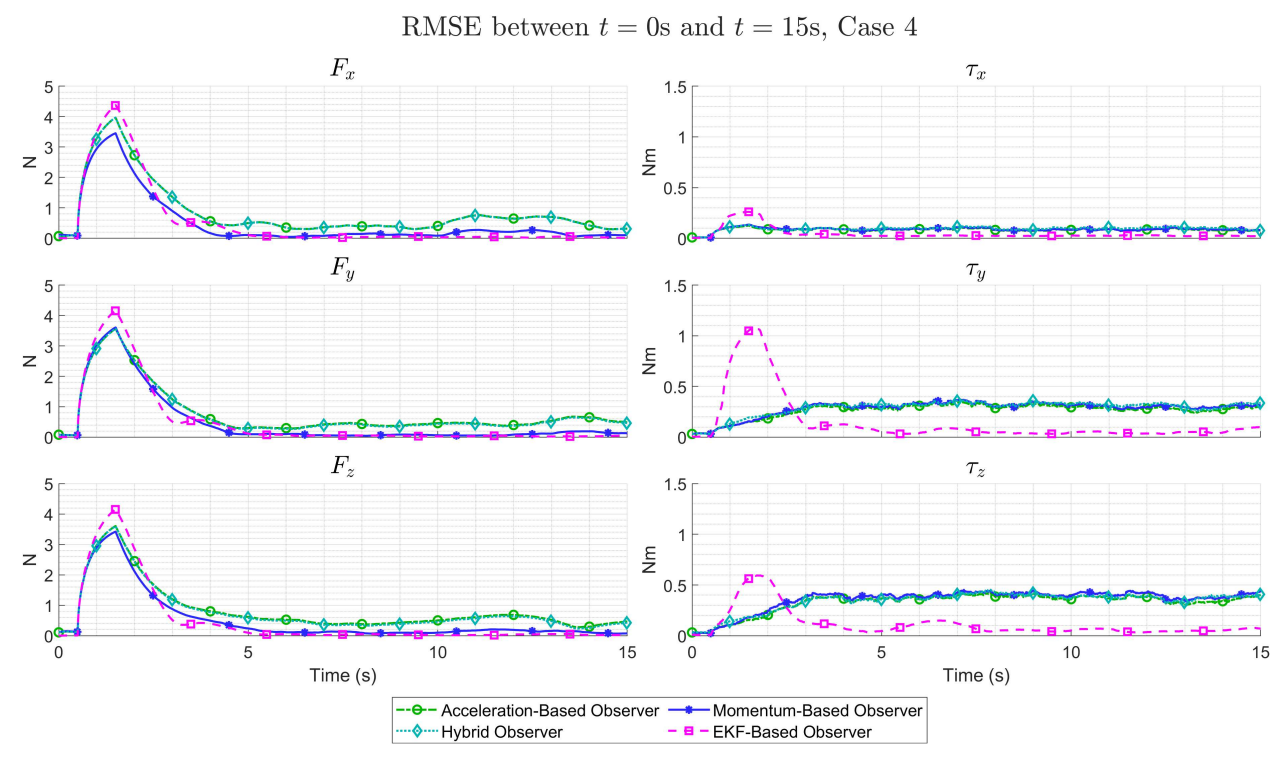


Fig. 23 RMSE using a 100 sample sliding window for Case 4.

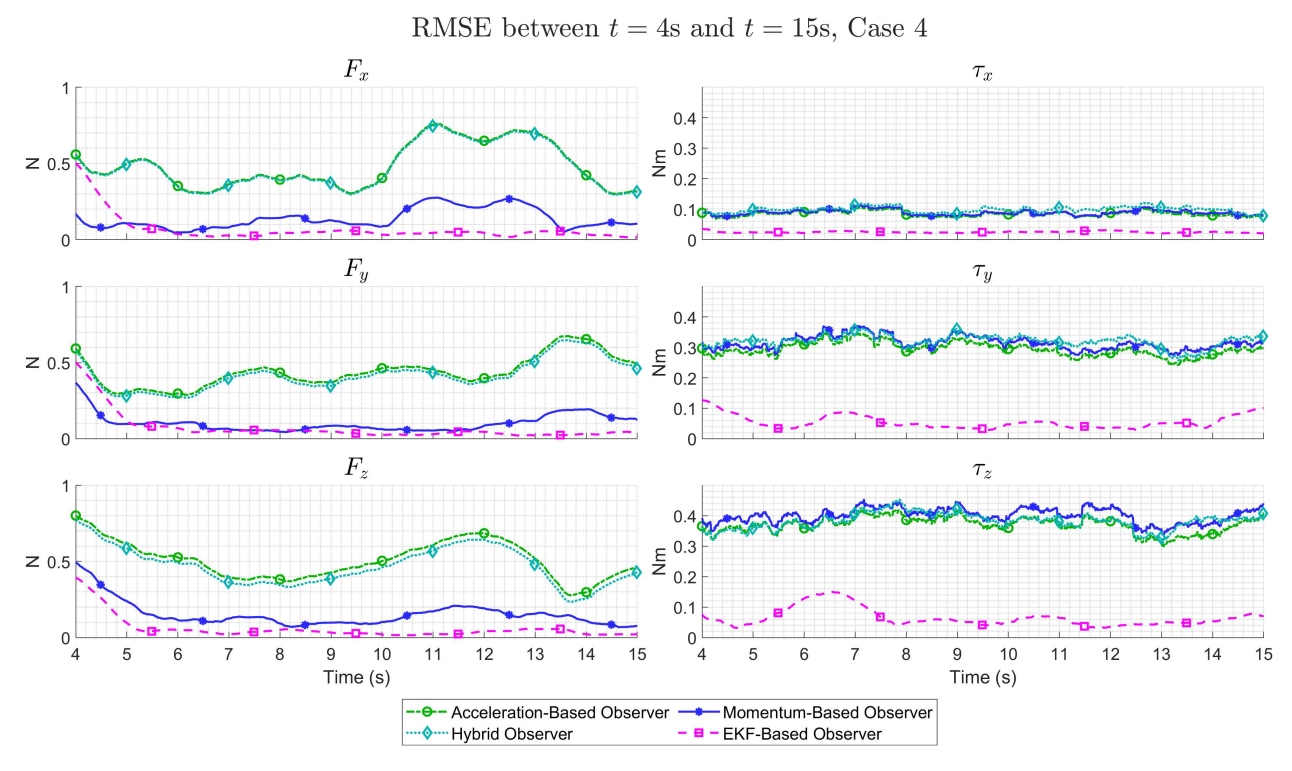
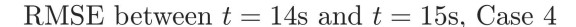


Fig. 24 RMSE using a 100 sample sliding window for Case 4 between t = 4s and t = 15s.



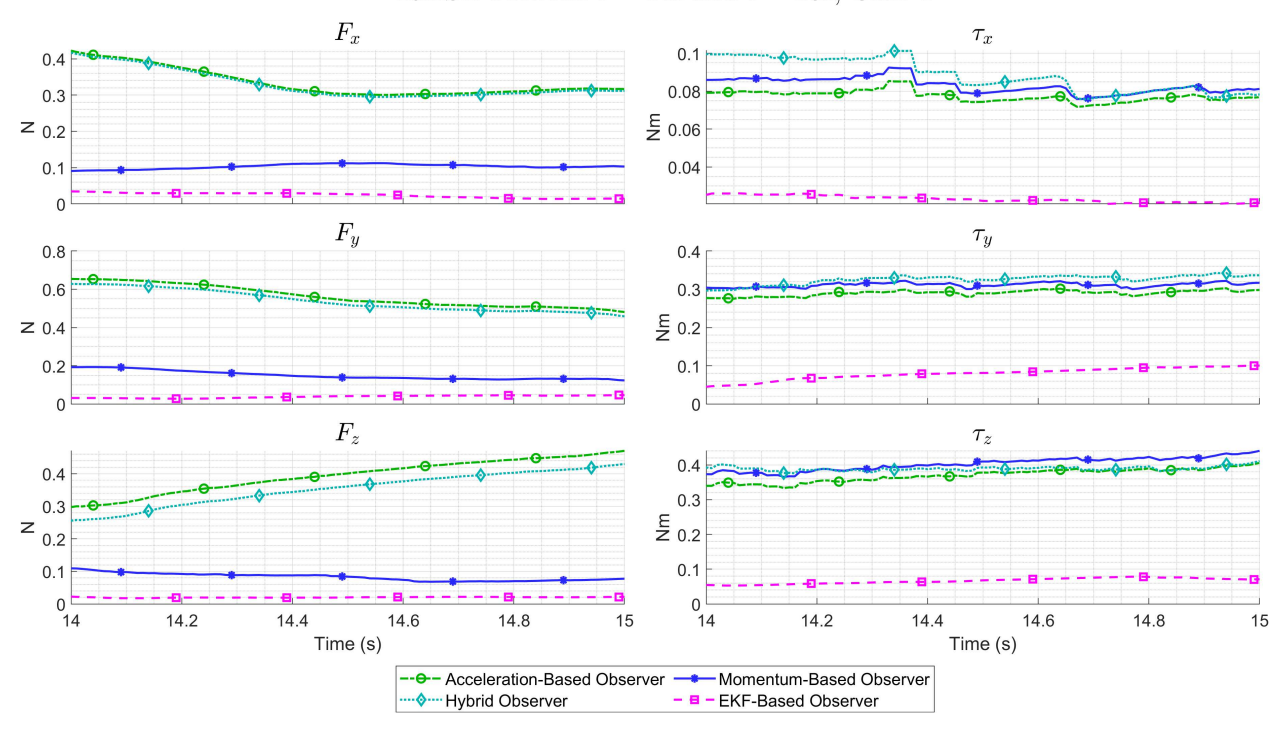


Fig. 25 RMSE using a 100 sample sliding window for Case 4 between t = 14s and t = 15s. Note that the y-axis limits for differ significantly, so that differences in RMSE can be seen with greater clarity.

- [10] Ruggiero, F., Cacace, J., Sadeghian, H., and Lippiello, V., "Passivity-based control of VToL UAVs with a momentum-based estimator of external wrench and unmodeled dynamics," *Robotics and Autonomous Systems*, Vol. 72, 2015, pp. 139–151.
- [11] Garrard, Y., Zhang, W., Inoyama, D., and Stoumbos, T. G., "Precision Control of a Quadrotor During Takeoff and Landing under the Ground Effect," *AIAA SCITECH 2022 Forum*, 2022, p. 1015.
- [12] Nigro, M., Pierri, F., and Caccavale, F., "Control of an Omnidirectional UAV for Transportation and Manipulation Tasks," *Applied Sciences*, Vol. 11, No. 22, 2021, p. 10991.
- [13] Rajappa, S., Bülthoff, H. H., Odelga, M., and Stegagno, P., "A control architecture for physical human-UAV interaction with a fully actuated hexarotor," 2017 IEEE/RSJ International Conference on Intelligent Robots and Systems (IROS), IEEE, 2017, pp. 4618–4625.
- [14] Ryll, M., Muscio, G., Pierri, F., Cataldi, E., Antonelli, G., Caccavale, F., Bicego, D., and Franchi, A., "6D interaction control with aerial robots: The flying end-effector paradigm," *The International Journal of Robotics Research*, Vol. 38, No. 9, 2019, pp. 1045–1062.
- [15] Brunner, M., Giacomini, L., Siegwart, R., and Tognon, M., "Energy tank-based policies for robust aerial physical interaction with moving objects," 2022 International Conference on Robotics and Automation (ICRA), IEEE, 2022, pp. 2054–2060.
- [16] Tomić, T., Ott, C., and Haddadin, S., "External wrench estimation, collision detection, and reflex reaction for flying robots," *IEEE Transactions on Robotics*, Vol. 33, No. 6, 2017, pp. 1467–1482.
- [17] Corsini, G., Jacquet, M., Jimenez-Cano, A. E., Afifi, A., Sidobre, D., and Franchi, A., "A general control architecture for visual servoing and physical interaction tasks for fully-actuated aerial vehicles," 2021 Aerial Robotic Systems Physically Interacting with the Environment (AIRPHARO), IEEE, 2021, pp. 1–8.
- [18] Schuster, M., Bernstein, D., Reck, P., Hamaza, S., and Beitelschmidt, M., "Automated Aerial Screwing with a Fully Actuated Aerial Manipulator," 2022 IEEE/RSJ International Conference on Intelligent Robots and Systems (IROS), IEEE, 2022, pp. 3340–3347.

- [19] Tomić, T., Lutz, P., Schmid, K., Mathers, A., and Haddadin, S., "Simultaneous contact and aerodynamic force estimation (s-cafe) for aerial robots," *The International Journal of Robotics Research*, Vol. 39, No. 6, 2020, pp. 688–728.
- [20] Liang, J., Chen, Y., Wu, Y., Zhong, H., Miao, Z., Zhang, H., and Wang, Y., "Active Physical Interaction Control for Aerial Manipulator Based on External Wrench Estimation," *IEEE/ASME Transactions on Mechatronics*, 2023.
- [21] Lee, S.-i., Kim, H., Kim, U., and Lee, H., "Concave wall surface tracking for aerial manipulator using contact force estimation algorithm," 2020 20th International Conference on Control, Automation and Systems (ICCAS), IEEE, 2020, pp. 850–855.
- [22] Wilmsen, M., Yao, C., Schuster, M., Li, S., and Janschek, K., "Nonlinear wrench observer design for an aerial manipulator," *IFAC-PapersOnLine*, Vol. 52, No. 22, 2019, pp. 1–6.
- [23] Lippiello, V., and Ruggiero, F., "Cartesian impedance control of a UAV with a robotic arm," *IFAC Proceedings Volumes*, Vol. 45, No. 22, 2012, pp. 704–709.
- [24] Tomić, T., Ott, C., and Haddadin, S., "External Wrench Estimation, Collision Detection, and Reflex Reaction for Flying Robots," *IEEE Transactions on Robotics*, Vol. 33, No. 6, 2017, pp. 1467–1482. https://doi.org/10.1109/TRO.2017.2750703, conference Name: IEEE Transactions on Robotics.
- [25] Patnaik, K., Saravanakumaran, A. A. P., and Zhang, W., "To Collide or Not To Collide–Exploiting Passive Deformable Quadrotors for Contact-Rich Tasks," *arXiv preprint arXiv:2305.17217*, 2023.
- [26] Khamseh, H. B., Ghorbani, S., and Janabi-Sharifi, F., "Unscented Kalman filter state estimation for manipulating unmanned aerial vehicles," *Aerospace Science and Technology*, Vol. 92, 2019, pp. 446–463.